

TECHNICAL REPORT

Open Access



A new five-wavelength photometer operated in Tromsø (69.6°N, 19.2°E)

Satonori Nozawa^{1*} , Tetsuya Kawabata¹, Keisuke Hosokawa², Yasunobu Ogawa³, Takuo Tsuda², Akira Mizuno¹, Ryoichi Fujii¹ and Chris Hall⁴

Abstract

A new five-wavelength photometer was developed and installed at the EISCAT Tromsø site (69.6°N, 19.2°E) in January 2017. The photometer consists of two units: an optical unit and a control unit together with a PC. The photometer is capable of simultaneously observing auroral emissions with five wavelengths. A uniqueness of the present system is its capability of precise pointing, which enables pointing the photometer at the field-aligned position using a star image obtained with a coaxial digital camera. Another uniqueness of the system is its capability of taking data at a sampling rate of 400 Hz. Some preliminary results including correlations between 427.8 nm and 557.7 nm, 630 nm, 777.4 nm, and 844.6 nm are presented. These comparisons are not significant unless all of the five wavelength emissions emanated from exactly the same volume (i.e., magnetic zenith) in the ionosphere, which the present system has.

Keywords: Auroral emission, Photometer, Field-aligned position, Tromsø

Introduction

The upper atmosphere in the polar region is significantly impacted by particle precipitation and the electric field originating from the magnetosphere. Great attention has been paid to auroral particle precipitation not only for the effect of ionizing and heating the polar thermosphere but also for its influence on the ozone distribution in the (upper) stratosphere (cf. Turunen et al. 2009; Isono et al. 2014). Photometric observations can be used to infer an average energy of the precipitating electrons, which leads to derivation of ionospheric conductivities, and deviation in the atmospheric composition induced by auroral heating (e.g., Gustavsson et al. 2001; Hecht et al. 1989, 1999; Robinson and Vondrak 1994; Vallance Jones and Gattinger 1990; Scourfield et al. 1971). The altitude of the lower border and the altitude of maximum emission depend strongly on the highest and typical energy levels of the precipitating electrons (Gustavsson et al. 2001). For example, the emission intensities at wavelengths of 427.8 nm (N_2^+ first negative band) and 630.0 nm

(metastable atomic state $O(^1D)$) have been used to infer the characteristic energies and energy fluxes of them (Adachi et al. 2017; Niciejewski et al. 1989; Strickland et al. 1989; Rees and Luckey 1974). The absolute emission rate of 427.8 nm radiation is related to the electron flux (Gustavsson et al. 2001; Rees and Luckey 1974), and the intensity ratio of 427.8–630.0 nm is related to the characteristic energy (e.g., Vondrak and Sears 1978). Furthermore, the 630 nm emission is sensitive to the oxygen concentration (Meier et al. 1989). For example, Hecht et al. (1999) used photometric observations of auroral emissions (427.8, 630.0, 844.6, and 871.0 nm) to derive atmospheric extinction, the average energy of the precipitating electrons, and the atmospheric composition induced by auroral heating.

Allowed transitions (e.g., 427.8 nm, 777.4 nm, 844.6 nm) correspond to a lifetime of the order of 10^{-8} s, while for forbidden transitions, a lifetime may range from milliseconds to hours; for example, the lifetime of the 557.7 nm emission is estimated to be about 0.75 s (Vallance Jones and Gattinger 1990; Vallance Jones 1974). For observations of a highly dynamic aurora with sub-second resolution, prompt emissions are needed. The most prominent atomic oxygen lines are the $3s\ ^5S-3p\ ^5P$ at 777.4 nm and $3s\ ^3S-3p\ ^3P$ at 844.6 nm (see Fig. 2

*Correspondence: nozawa@nagoya-u.jp

¹ Institute for Space-Earth Environmental Research, Nagoya University, Furo-cho, Chikusa-ku, Nagoya, Japan

Full list of author information is available at the end of the article

of Lanchester et al. 2009). The 777.4 and 844.6 nm lines result from an allowed transition in atomic oxygen (Vallance Jones and Gattinger 1990; Lummerzheim et al. 1990). They have excitation thresholds above 10 eV and therefore are most suitable for characterizing low energy precipitation (Lanchester et al. 2009). The 777.4 nm line is a multiplet: 777.196 nm, 777.418 nm, and 777.54 nm (Hecht et al. 1985). The 844.6 emission is also a multiplet that consists of three lines at 844.636, 844.638, and 844.676 nm (Hecht et al. 1985; Krassovsky et al. 1962).

It should be noted that the photometer measurements, like other single-point measurements, have an unavoidable weakness. The time variation of emissions integrated along the magnetic field line is a partial differential value with time and a mixture of the temporal and the spatial variations, and hence it is not possible to differentiate between the two variations only from the photometer observation. To overcome this point, a highly sensitive all-sky imager has been operative at the same location, which would yield both temporal and spatial distribution of the aurora around the position where the photometer measures. The all-sky imager is equipped with EMCCD camera which enables us to observe the 2D structure of aurora at a temporal resolution of 100 Hz. These two measurements are complementary, that is, the photometer is capable of providing the (1) the absolute amount of (2) several wavelengths emissions with (3) very fast samplings, all of which are difficult for the present all-sky imager to provide.

A four-wavelength photometer was operated at the EISCAT (Folkestad et al. 1983) Tromsø site (69.6°N, 19.2°E) between 2002 and 2016, and data were used for derivation of the conductivities (e.g., Adachi et al. 2017; Oyama et al. 2013) and monitoring the auroral activity (e.g., Takahashi et al. 2015). Adachi et al. (2017) compared height-integrated conductivities derived from the EISCAT radar measurements and the photometer operated at Tromsø. They used 427.8 nm and 630 nm emissions for derivation of characteristic energy and flux of the auroral particle electrons and derived ionospheric conductivities. Although the photometer measurements tended to underestimate conductances, they showed a good agreement in temporal variations of height-integrated conductivities (i.e., conductances) between the two methods, suggesting usefulness of photometer measurements. Furthermore, photometer measurements provide important information on auroral activities.

First, reasons for the choice of five wavelengths are presented, and new features of the new photometer are emphasized. Second, we present some observational results: Differences in temporal variations between 427.8 nm emission and the other emissions (557.7, 630, 777.4, and 844.6 nm) are paid attention. Possible

candidates which cause a rapid response of the 630 nm emission are mentioned in the discussion section. Finally, this paper ends with a summary and conclusion.

Choice of five wavelengths

We have adopted the following emissions: 427.8, 557.7, 630.0, 777.4, and 844.6 nm. As already mentioned, the 427.8 nm emission is directly related to the electron flux (Gustavsson et al. 2001; Rees and Luckey 1974), and a combination of the 427.8 nm with any of the 630, 777.4, or 844.6 nm emissions will enable deriving a characteristic energy of precipitating electrons (Adachi et al. 2017; Lanchester et al. 2009). The 557.7 nm emission is the brightest line among those, about five times more intense than that of the 427.8 nm emission. Thus, the 557.7 nm emission is most effectively used for the study of less bright pulsating auroras. Furthermore, time lag between 427.8 and 557.7 nm emissions can be used for derivation of change of molecular oxygen (cf. Scourfield et al. 1971), while time delay of 630 nm can be used for derivation of change of atomic oxygen (cf. Kalogerakis et al. 2009). For derivation of the characteristic energy of auroras which rapidly vary in intensity, such as pulsating auroras, the allowed lines (777.4 and 844.6 nm) are a better choice than the 630 nm emission.

New capabilities of the photometer

The present photometer has two new features compared to the previous one. One is a pointing capability for ensuring the field-aligned measurements. For incident electron energies greater than a few keV, the auroral spectrum is dominated by the oxygen green line at 557.7 nm and by the band systems of N_2 and N_2^+ , with the total luminosity proportional to net energy flux, while the higher altitude emissions of O and O^+ become increasingly significant when the characteristic energy (E_0) decreases (Semeter et al. 2001). Under these circumstances, 427.8 and 557.7 nm emissions predominantly emanate in the lower thermosphere (about 90–130 km), while 630, 777.4, and 844.6 nm emissions mainly emanate in the thermosphere (above about 200 km). The difference of heights should be considered carefully and taken seriously when using multiple emissions to derive the energy of the precipitation auroral electrons. Field-aligned measurements are essential because the auroral electrons precipitate along the field lines. In other directions, the observed ratios of two emissions cannot be directly related to energy in a simple way (Vallance Jones and Gattinger 1990).

Another new feature is its fast data sampling. The present photometer is capable of yielding data with the maximum sampling rate of 400 Hz/channel, giving meaningful information below the Nyquist frequency,

$400/2=200$ Hz. Such a fast sampling enables us to discover fast varying phenomena that have never been possible to identify before. For example, more than 10 Hz rapid modulations that are considered to be embedded in pulsating auroras have not yet been observationally confirmed by optical instruments.

Optical unit

The photometer consists of two units: an optical unit and a control unit with a PC. Figure 1a illustrates a schematic diagram of the optical unit of the photometer. The optical unit consists of a head part, four dichroic mirrors, five optical bandpass filters, five photomultiplier tubes (PMTs), and several kinds of lenses and mirrors. The elevation angle of the head part can be adjusted by an elevation adjuster.

A digital camera can be attached for pointing of the photometer. Figure 1b depicts the optical unit of the photometer in more detail, and Table 1 summarizes parameters of the optical devices used with numbers shown in the figure. The size of the optical part (except for the head part) is 509 mm (400 mm) \times 200 mm \times 110 mm (H). In Fig. 1b, the auroral light comes into the photometer through the head part on the left side of the figure: the head part uses a lens (No. 1) and a prism mirror (No. 2). The incident light is focused at a pinhole (No. 4) with the two lenses (No. 1, and 3), expands after passing through the pinhole, and is collimated with a lens (No. 5). The diameter of the pinhole is 2 mm which determines, together with the lenses (No. 1 and 3), the field of view (FOV), more precisely the “receiving area,” of the photometer to be about 0.98 degrees. The FOV size is chosen to be close to that of the EISCAT_3D radar (Tsuda et al. 2016) for future simultaneous observations. Passing through the lens (No. 5), the incident light is split by dichroic mirrors (No. 6, 7, 8, 9); the first, second, and fourth dichroic mirrors are long-pass filter types, and the third one is a short-pass filter type. Five sets of bandpass filters (No. 14, 15, 16, 17, 18) and PMTs are used for simultaneous measurements of five-wavelength auroral lights. Just before entering into PMTs, sets of lenses (No. 19 or 20) adjust the beam width of the incident light to the acceptance surface of the PMTs. Regarding the pointing of the photometer, the incident light is reflected perpendicularly except for the light into the pinhole (No. 4). The reflected light passes through a field lens (No. 11) is collimated with the lens (No. 12) and is used for pointing with a coaxial digital camera. To show more clearly how the incident light is split and led into the PMTs, Fig. 1c depicts distribution of the dichroic mirrors. The 1st dichroic mirror reflects 97% of the incident light with wavelengths of 350–480 nm, while it passes about 85% of the incident light with wavelengths of 520–1600 nm.

The second dichroic mirror reflects 97% of the incident light with wavelengths of 460–570 nm, while it passes about 85% of the incident light with wavelengths of 625–1600 nm. Consequently, passing through the two dichroic mirrors, the intensity of the incident light is depreciated by about 30%. Ch1 and Ch2 are used for measurements of 427.8 nm and 557.7 nm emissions, respectively. The third dichroic mirror passes about 80% of the incident light with a wavelength of 400–680 nm: The passing light is used for measurements of 630 nm or 664.6 nm. The bandpass filter before the PMT (Ch3) can be easily replaced, so we can replace one of the filters easily with another on site. The 4th (last) dichroic mirror reflects 98% of the incident light with a wavelength of 450–790 nm, and Ch4 is used for measurements of 777.4 nm emission. The passing light (90%) is used for measurements of 844.6 nm at Ch5. The bandpass filters used are summarized in Table 2. The full width at half maximum (FWHM) of the filters is 2 nm except for 777.4 nm (2.5 nm) and 664.6 nm (13 nm), and the shapes of the transmittance of all the filters are mostly trapezoid. Usually targeted wavelengths are located around the center of the filter transmission area except for the filter for 777.4 nm. To avoid possible contamination from molecule nitrogen lines (i.e., 775.37 and 775.2 nm), a filter centered at 777.9 nm is used. At channel 3, a filter of 664.6 nm was used before April 16, 2017, and then a filter of 630 nm was used between September 6, 2017, and March 22, 2018. The filters used in the photometer are made by Andover Inc. with a diameter of about 25 mm, an effective diameter of 21 mm, and a thickness of about 7 mm.

Pointing capability of the photometer

One of the major improvements in this new photometer as already mentioned is a pointing capability using star images obtained with a coaxial digital camera. Figure 2a depicts the schematic diagram of the divider part (No. 4 in Fig. 1b), Fig. 2b shows its cross-section diagram. The diameter of the pinhole is 2 mm, and the optic axis of the pinhole is pointed to be parallel to the incident light from the prism mirror and lenses (No. 1 and 3 in Fig. 1b). The diameter of the outer circle of the pinhole part is 4.5 mm, and some of the incident light is lost when entering into the area between the outer circle and outside of the pinhole. The incident light, except for that entering the outer circle (diameter 4.5 mm), is reflected by the mirror for the input for a coaxial digital camera.

Figure 3 shows a star image obtained with a digital camera (Nikon D5200) with an exposure time of 10 s at 19:51:20 UT on September 28, 2017, on the right, together with a star image from the astronomical software (StellaNavigator8 produced by AstroArts Inc.) at

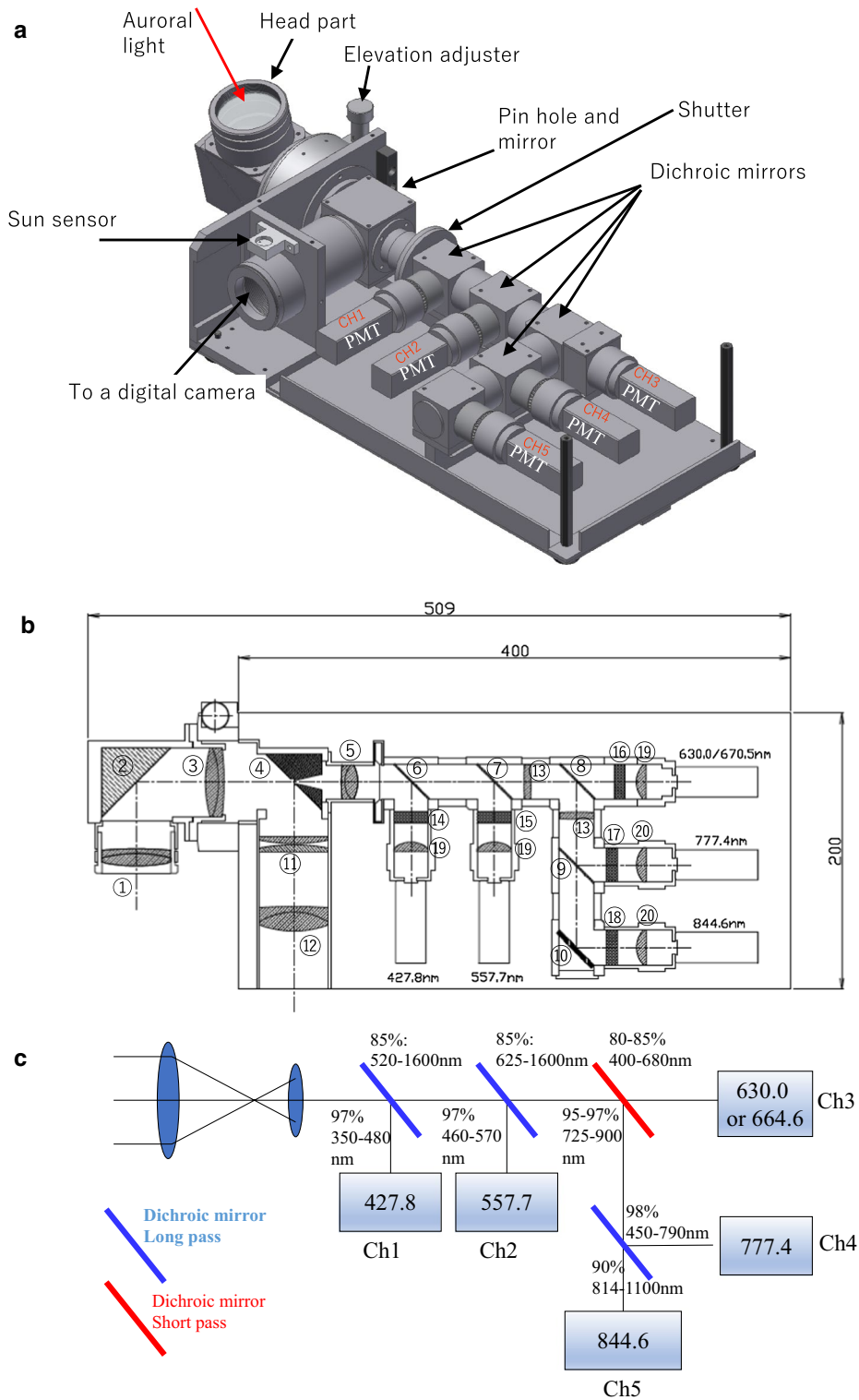


Fig. 1 **a** Schematic diagram of the optical unit of the photometer. **b** Block diagram of the optical part of the photometer. Unit is in mm. **c** Schematic diagram of distribution of the dichroic mirrors of the photometer. Penetration and reflection efficiencies of the dichroic mirrors with corresponding wavelength intervals are shown

Table 1 List of optical devices

No.	Device type	Comments; unit is in mm
1	Lens	D50 f200
2	Prism mirror	Enhanced aluminum coated
3	Lens	D50 f150
4	Mirror	56.57 × 40 (with pinhole)
5	Lens	D25 f40
6,7,8,9	Dichroic mirror	25.2 × 35
10	Mirror	25 × 35; protected gold
11	Lens	D50 f250
12	Lens	D50 f100
13	Lens	D25 f400
14,15,16,17,18	Bandpass filter	See Table 2
19	Lens	D25 f35
20	Lens	D25 f30

the same time on the left. Stars which are brighter than a magnitude of 10 are shown. The black-filled solid circle around the center of the image on the right side (i.e., the image of the digital camera) corresponds to the area where the incident light is used for the photometer itself as well as the light lost due to the design (see above). The white cross on the left image indicates the local field-aligned position (i.e., Azimuth = 187.1° and Elevation = 77.6°). We compare the two images in terms of distribution of stars. Although shapes of stars are a bit distorted in the image taken with the digital camera, we can compare the two images well. Thus, we claim that the photometer observed auroral emissions along the local field line (i.e., magnetic zenith).

Table 2 List of bandpass filters produced by Andover Inc.

	Center wavelength (error)	FWHM* (error)	Numbers in Fig. 1b	Targeted auroral emissions
Ch1	427.8 nm (+0.4/−0 nm)	2.0 nm (±0.5 nm)	14	N ₂ ⁺ 1NG:427.8 nm
Ch2	557.7 nm (+0.4/−0 nm)	2.0 nm (±0.5 nm)	15	OI(1S): 557.7 nm
Ch3	630.0 nm (+0.4/−0 nm)	2.0 nm (±0.5 nm)	16	OI(1D): 630.0 nm
Ch3	664.6 nm (±2.0 nm)	13 nm (±3.0 nm)	16	N ₂ 1PG: 664.6 nm
Ch4	777.9 nm (+0.4/−0 nm)	2.5 nm (±0.5 nm)	17	OI(3p ⁵ P): 777.4 nm
Ch5	844.6 nm (+0.4/−0 nm)	2.0 nm (±0.5 nm)	18	OI(3p ³ P): 844.6 nm

*FWHM: Full width at half maximum

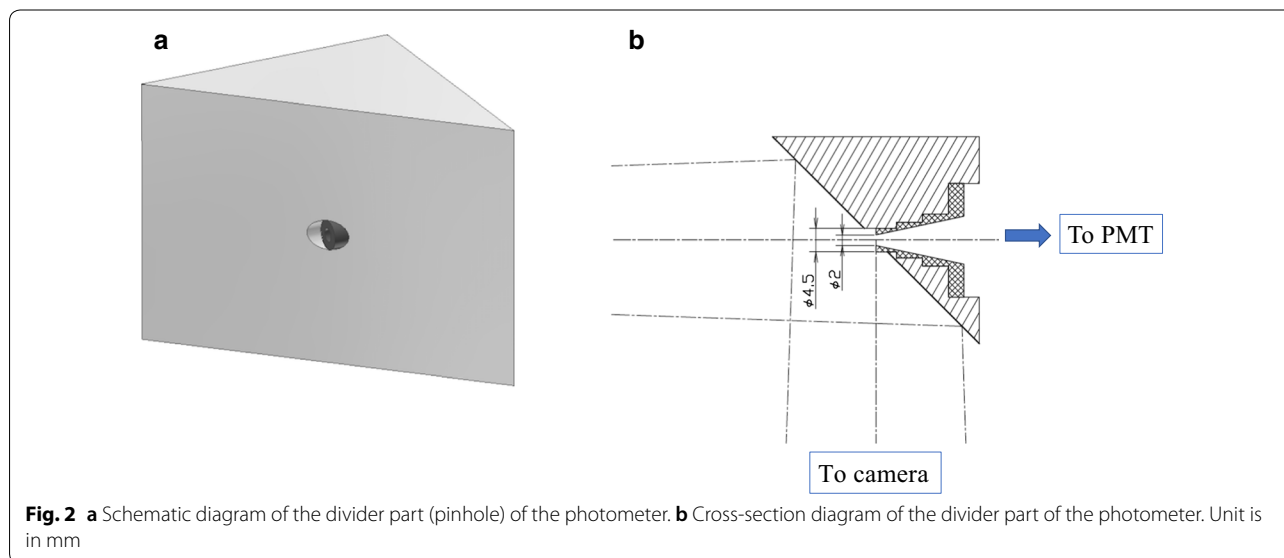


Fig. 2 a Schematic diagram of the divider part (pinhole) of the photometer. b Cross-section diagram of the divider part of the photometer. Unit is in mm

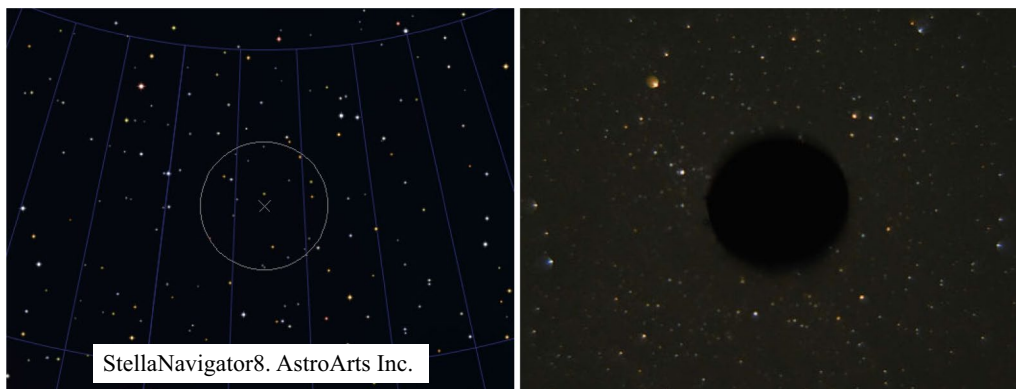


Fig. 3 A star chart (left) and a sky image (right) obtained by digital camera with an exposure time of 10 s at 19:51:20 UT on September 28, 2017. The cross on the left chart denotes the position of the local field-aligned position (Azimuth = 187.1° and Elevation = 77.6°). The diameter of the circle on the left is 2 degrees, and the field of view of the star images are about 8° × 6°

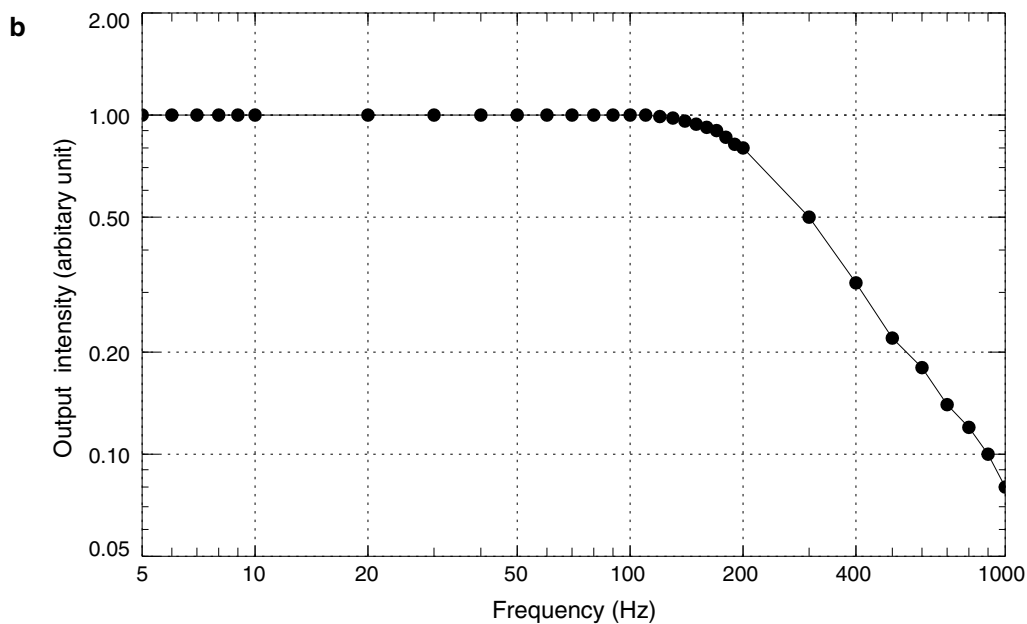
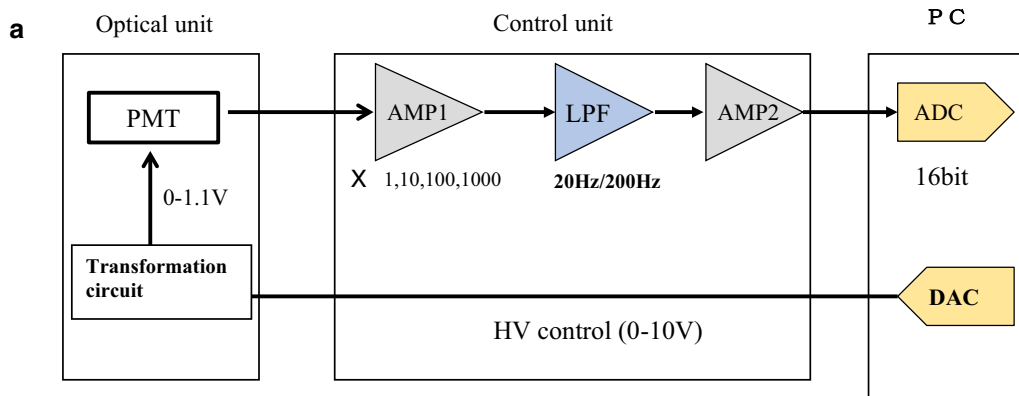


Fig. 4 a Schematic diagram of the signal processing in the optical unit, control unit, and PC. **b** Response of the control unit (Ch1) with a low-pass filter of 200 Hz as function of frequency. Output intensity is normalized

Control unit

The control unit of the photometer is stored in a box (150 mm (H) X 320 mm (W) X 330 mm (D)). Figure 4a depicts a schematic diagram showing how the signal from a PMT is treated and is led into an A/D converter (ADC) on the board in the PC, as well as how gains of PMTs are controlled by PC. Signal gains are controlled in two ways: One is by using an amplifier (AMP1), and the other is using PMT high voltage (HV) controlled by PC through D/A converter (DAC). In general, first we choose an amplifier module (AMP1) at each channel and then control input voltage to PMTs by checking signal intensities based on auroral observations. We have made four kinds of amplifier modules (gains being amplified by 1, 10, 100, and 1000), and we select one for each channel depending on intensity of auroral emissions. The amplifier module (AMP1) also adjusts the voltage offset. We used 100, 10, 10, 10, and 100 times gain between February 1 and April 16, 2017, and 100, 10, 10, 100, and 1000 times gain between September 6, 2017, and March 22, 2018, respectively, for Ch1 (427.8 nm), 2 (557.7 nm), 3 (664.6 nm or 630 nm), 4 (777.4 nm), and 5 (844.6 nm). The amplifier modules are integral calculus inversion amplification circuits. The signal from a PMT is amplified at the first amplifier module (AMP1) and then passes through a low-pass filter (LPF). Regarding the low-pass filter, the cutoff frequency of either 20 Hz or 200 Hz can be chosen. Twenty Hertz between February 1 and April 16, 2017, and 200 Hz between September 6, 2017, and March 22, 2018, were used. Then, the signal is led into the second amplifier module (AMP2; no amplification is made here, but the signal is inverted in voltage) and then led into an A/D converter (ADC; 16 bit, 5 micro-sec/channel) installed in the computer (PC: ITC-N3620, Interface Corporation). The computer acquires data from the photometer in this way and also controls high voltage (HV) levels of the PMTs by sending signals through a D/A converter (DAC). Concerning the PMTs, H11902-210 for Ch1 is used and H11902-20 is used for the other channels; all the PMTs are produced by Hamamatsu Photonics K.K. Gains of the PMTs are controlled by input voltage that ranges from +0.5 to 1.1 V. The input voltage is controlled by the observational program using HV setting values ranging from 0 to 100 (arbitrary unit). The voltage signal from DAC ranging from 0 to 10 V is sent to the transformation circuit inside the optical unit, and then the circuit transforms the voltage signal to a lower signal level between 0 and 1.1 V. When a HV value is increased by 5 under conditions where HV values are greater than 50, the gain is roughly doubled. We set HV values as 75, 75, 75, 80, and 75 between September 6 to 19, 2017, and 75, 75, 80, 80, and 75 between September 20, 2017, and March 22, 2018, for Ch1, 2, 3, 4, and 5,

respectively. Figure 4b depicts the response of the control unit (in the case of Ch1) with a low-pass filter of 200 Hz to input signals with frequency between 5 and 1000 Hz. Almost no loss of the input signal at less than 100 Hz is found, showing that obtained data can be used for analysis of high-frequency variation of auroral emissions such as pulsating auroras.

Observational scheme

The observational program of the photometer is written in C language. The observational procedure is as follows: (1) power on the photometer system with zero voltage applied to the PMTs and amplifiers, (2) obtain dark level data at the beginning of the observation for 20 min with high voltage (HV) loaded on the PMTs, (3) obtain sky data (i.e., measurements of auroral light), (4) once an hour, obtain dark level data for 10 s, (5) obtain dark level data for 10 min at the end of the observation, (6) apply zero voltage on the PMTs and amplifiers, and (7) power off the system. We obtained data at a 400 Hz sampling rate between September 6, 2017, and March 22, 2018, and at 20 Hz between February 1 and April 16, 2017. A shutter device was installed during the summer season (i.e., between May and August 2017); before then, we did not obtain dark level data.

The digital camera (Nikon D7200) automatically made all-sky image observations every day (http://www.isee.nagoya-u.ac.jp/~eiscat/obs/d5000/html/sky_image.html) between September 6, 2017, and March 22, 2018. The observation program was written in C and Visual Basic languages. Sky images were taken every 30 s with an exposure time of 8 s, except for the first and last intervals of 1 h each. During these intervals, the exposure time was set to 1 s because of a brighter sky.

Finally, Table 3 summarizes information on PMTs, amplifier values in AMP1, and HV setting values used between September 20, 2017, and March 22, 2018. In addition, standard deviation values (in Rayleigh) of dark noise levels on the night of October 19, 2017, are listed for 20 Hz and 1 s data. In Table 3, those on the night of January 22, 2018, are presented.

Results

Here, in order to prove performance of the photometer, we present temporal variations as examples of auroral emissions obtained with the photometer on two nights. On both of the two nights, the auroral activity was high: Auroral arcs appeared in the evening sector, and diffuse and pulsating auroras appeared in the morning sector. We also present comparison of temporal variations of the 427.8 nm emission with the others (557.7, 630, 777.4, and 844.6 nm).

Table 3 Standard deviation values (R) of dark noise together with information on PMT, AMP1, and HV values on (a) October 19, 2017, (b) January 22, 2018

	Ch1 (427.8)	Ch2 (557.7)	Ch3 (630)	Ch4 (777.4)	Ch5 (844.6)
a					
PMT*	H11902-210	H11902-20	H11902-20	H11902-20	H11902-20
AMP1(times)	100	10	10	100	1000
HV (arbitrary unit)	75	75	80	80	75
Dark noise (20 Hz) (R)	1.3	19.1	19.0	43.1	97.5
Dark noise (1 s) (R)	0.7	5.3	4.8	10.4	23.6
b					
Dark noise (20 Hz) (R)	1.5	13.2	13.9	29.3	66.0
Dark noise (1 s) (R)	1.1	2.8	2.9	6.3	14.6

*Produced by Hamamatsu Photonics K.K

Case 1: October 19, 2017

Figure 5 shows photometer data with five wavelengths obtained between about 16:34 UT on October 19 and about 04:25 UT on October 20, 2017. On that night, there was a clear sky after about 16:44 UT. The auroral activity was high and auroral emissions showed sharp rises of luminosity at several times between 16:56 UT and 21:00 UT. On the other hand, pulsating auroral features could be found in the morning sector between about 01 and 04 UT. The photometer observed auroral emissions at five wavelengths: 427.8 nm (N_2^+ first negative), 557.7 nm (OI (1S)), 630 nm (OI (1D)), 777.4 nm OI($3p^3P$), and 844.6 nm (OI($3p^3P$)) at a 400 Hz sampling rate. These temporal variations of luminosity with 1 s of averaged data are presented from top to down, respectively, in Fig. 5. At around 20:16 UT, an auroral breakup occurred. To show temporal and spatial development of auroral forms, nine all-sky images taken by digital camera (Nikon D7200) every 30 s with an exposure time of 8 s between 20:14:39 and 20:18:39 UT (time is a start time of the exposure) are shown in Fig. 6. The field-aligned position is indicated by a red plus sign (+). Figure 7 shows temporal variations of luminosity with 0.05 s (i.e., 20 Hz) resolution between 20:16:48 and 20:16:59 UT when the auroral emissions were at maximum at all the channels. In particular, we focus on the time difference between the 427.8 nm emission and the others (557.7, 630, 777.4, and 844.6 nm). Due to difference of luminosity, the luminosity values of 557.7, 630, 777.4, and 844.6 nm emissions were multiplied by 0.1, 5, 2, and 2, respectively. Comparing emissions of 427.8 nm and 557.7 nm, the 557.7 nm emission was delayed (as expected) because the 557.7 nm line is a forbidden line and takes about 0.75 s (depending on quenching effect) to emit photons. The temporal variations between 427.8 nm and 777.4 or 844.6 nm lines are very similar, because these are prompt emissions (cf. Semeter et al. 2001; Lanchester et al. 2009).

It is a bit surprising to see a difference of temporal variations of 427.8 nm and 630 nm emissions. There seems to be no time difference at the sharp rise of emissions at about 20:16:50 UT, although the 630 emission (OI (1D)) has a long radiative lifetime (about 40–120 s; cf. Ono and Hirasawa 1992, Semeter et al. 2001). We will consider this issue later in the discussion section. Time differences between two lines are more clearly seen in Fig. 8, showing scatter plots between 427.8 nm and 557.7 nm (top-left) or 630 nm (top-right) or 777.4 nm (bottom-left) or 844.6 nm (bottom-right). The correlation between 427.8 nm and 557.7 nm is the worst (correlation coefficient = 0.56) as shown on the top-left in Fig. 8, while the other emissions show a good correlation with 427.8 nm. Figure 9 compares temporal variations (20 Hz data) of auroral luminosities (557.7, 630, 777.4, and 844.6 nm) (red solid lines) with 427.8 nm (black solid lines) luminosities for 3 min between 20:57:00 and 21:00:00 UT on the same night. During the interval, rapid rises of the intensity of the 427.8 nm emission are seen at several times. Time differences are seen between 427.8 nm and 557.7 nm or 630 nm, and the temporal variations as well as luminosities are very similar to each other between 427.8, 777.4, and 844.6 nm.

In the morning sector, pulsating auroras appeared as shown in Fig. 5. Figure 10 shows temporal variations of auroral luminosities (20 Hz data used) at 557.7, 630, 777.4, and 844.6 nm together with overplotting of 427.8 nm emission intensity for 2 min between 01:06:00 and 01:08:00 UT on October 20, 2017. The emission of 427.8 nm shows clearly a pulsating auroral feature, and also the other emissions show similar variations except for the emission of 630 nm. Figure 11 shows spectra of auroral emissions at the five wavelengths, derived by the Lomb–Scargle method which is based on the least-squares frequency analysis of unequally spaced data (see

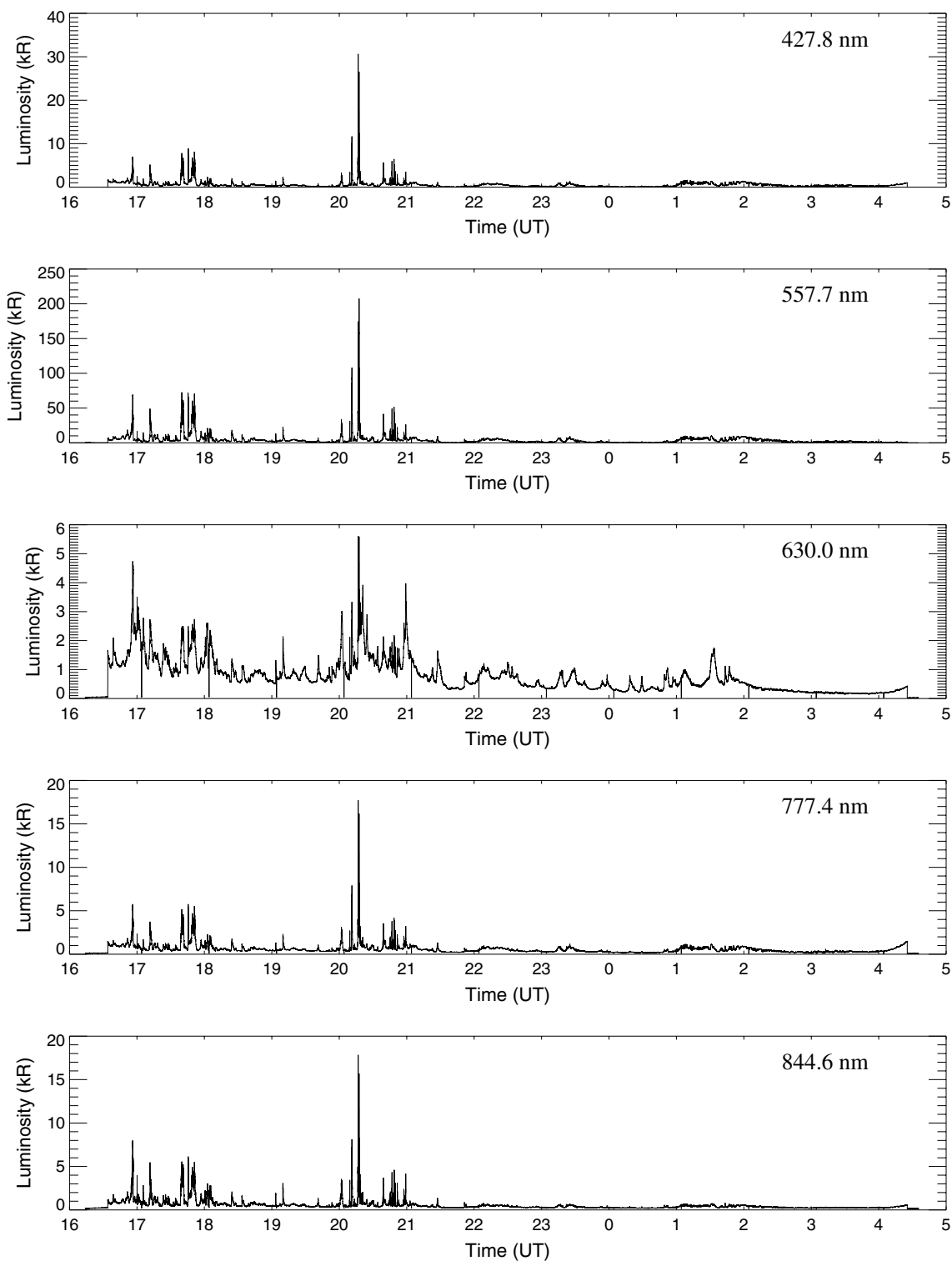


Fig. 5 Temporal variations of the auroral emissions obtained with the photometer with five wavelengths between about 16:34 UT on October 19 and about 04:25 UT on October 20, 2017. The emissions of 427.8 nm, 557.7 nm, 630 nm, 777.4 nm, and 844.6 nm (1 s of averaged data) are presented from top to bottom

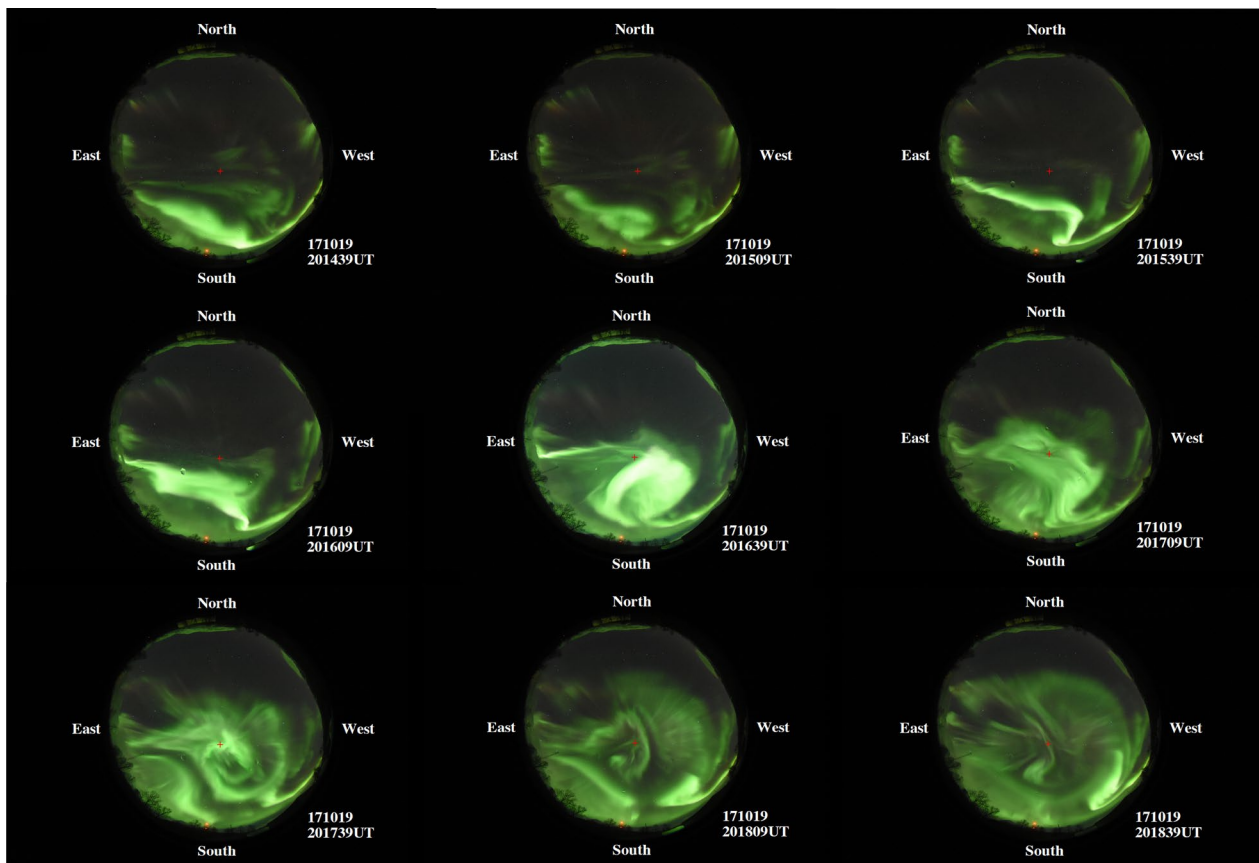


Fig. 6 All-sky images taken with a digital camera (Nikon D7200) every 30 s with an exposure time of 8 s between 20:14:39 UT and 20:19:39 UT on October 19, 2017. The field-aligned position, where the photometer was pointed, was indicated by a red plus sign (+)

Press and Rybicki 1989; Hocke 1998). The horizontal dashed lines denote the 99% significance level. At all the emissions, they show clear peaks at 1/5, 1/9.1, 1/11, and 1/20 Hz (i.e., corresponding to periods of 5, 9.1, 11, and 20 s, respectively) shown by vertical dotted lines. These oscillations lasted for several seconds to several minutes, and dominant periods varied with time. On the other hand, longer oscillations were also found. For example, Fig. 12 shows spectra derived from auroral emission data for 30 min between 01:30 and 02:00 UT on October 20, 2017. In this case, oscillation with a period of 225 s was dominant except for 630 nm where a period of 200 s was dominant. These results prove the photometer will provide good data sets for studies of pulsating auroras.

Case 2: January 22, 2018

Figure 13 shows temporal variations of auroral emissions at the five wavelengths with 1 s of averaged data over

the night between about 15:16 UT on January 22 and about 06:35 UT on January 23, 2018. It was partly cloudy until 18:50 UT on January 22, but then the sky cleared and remained clear until the end of the observation. The auroral activity was high between about 18 and 20 UT, and then pulsating auroras appeared in the morning sector between about 01 and 05 UT on January 23. Figure 14 compares temporal variations of the 427.8 nm (black solid lines) and 557.7, 630, 777.4, and 844.6 nm (red solid lines) for 2 min between 19:43:00 and 19:45:00 UT, and Fig. 15 shows scatter plots between 427.8 nm and the other four emissions. Here 20 Hz data are presented. Figure 16 shows four sky images between 19:43:10 and 19:44:40 UT every 30 s with an 8 s exposure time. During the interval, several bright discrete auroras showed up above Tromsø and covered FOV of the photometer. In Fig. 14, it is a bit surprising that no timing differences of the emissions between 427.8 nm and 630 nm are seen.

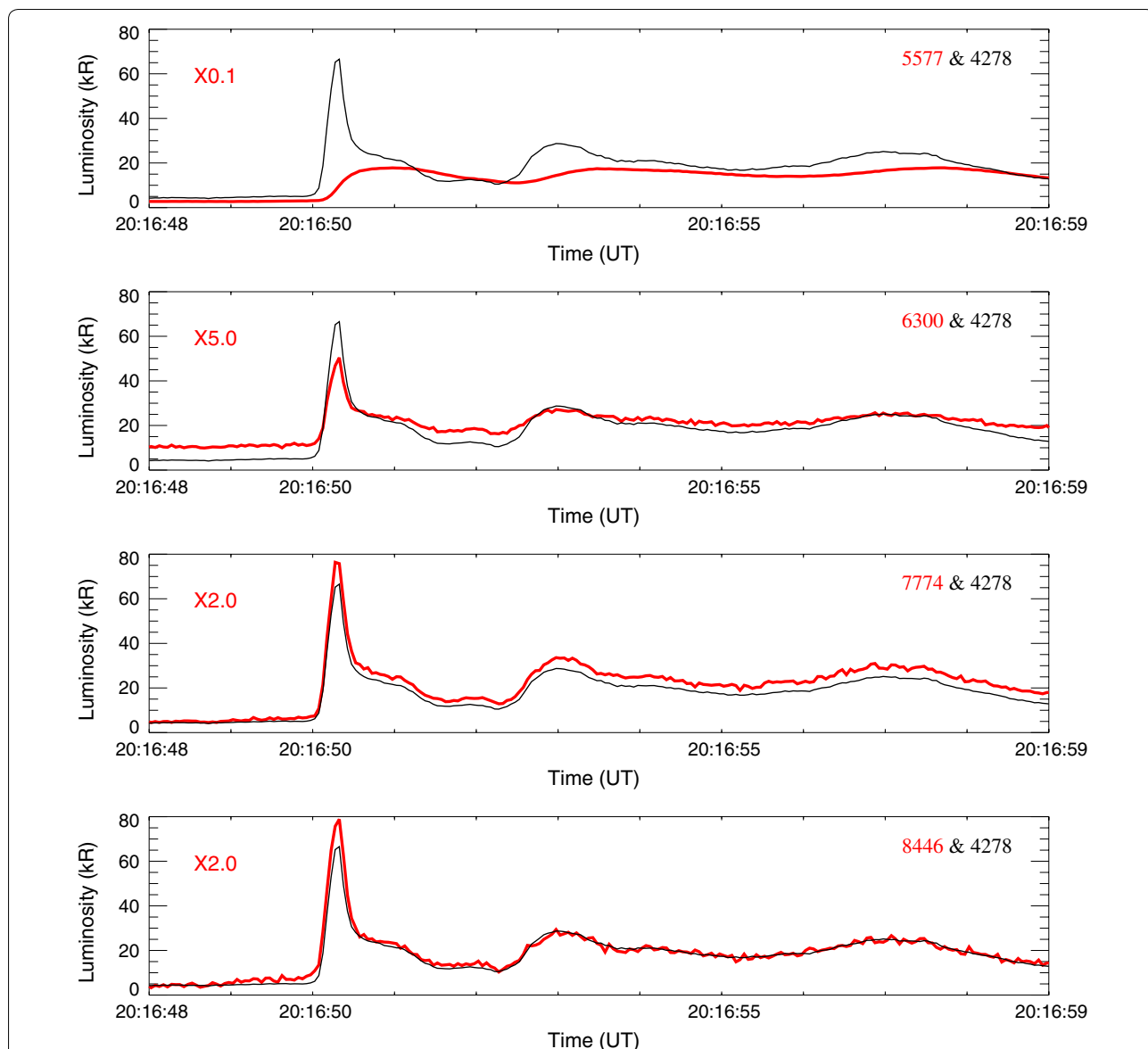


Fig. 7 Comparisons of temporal variations of auroral emissions (20 Hz data) between 427.8 nm (black solid line) and 557.7 nm, 630 nm, 777.4 nm, and 844.6 nm from top to bottom are presented for 11 s between 20:16:48 UT and 20:16:59 UT on October 19, 2017. The emission intensity values of 557.7 nm, 630 nm, 777.4 nm, and 844.6 nm are multiplied by 0.1, 5, 2, and 2, respectively, and denoted in red solid lines

Figure 15, scatter plots, also shows good correlations between 427.8 nm and the other emissions except for the 557.7 nm emission. Although the cross-correlation value between the two emissions of 427.8 and 557.7 nm is 0.98, there seems to be some temporal difference between the two lines, but it is not clear compared to the other case of Fig. 8.

Figure 17 shows comparisons of temporal variations of emissions between 427.8 nm and 557.7 nm, 630 nm, 777.4 nm, and 844.6 nm from top to down for 1 min between 22:33:00 UT and 22:34:00 UT. The 557.7 nm

emission was delayed by about (less than) 1 s, and the 630 nm emission also shows some delay. The other two lines, 777.4 and 844.6 nm, show very similar temporal variations with 427.8 nm emission. Figure 18 shows scatter plots and shows a clearly different response of the 557.7 nm emission against the 427.8 nm emission, although the cross-correlation value is high (0.96). The 630 nm emission also shows a different response from the 427.8 nm emission.

In the morning sector, pulsating auroras with relatively dark luminosity appeared and lasted for about 3–4 h.

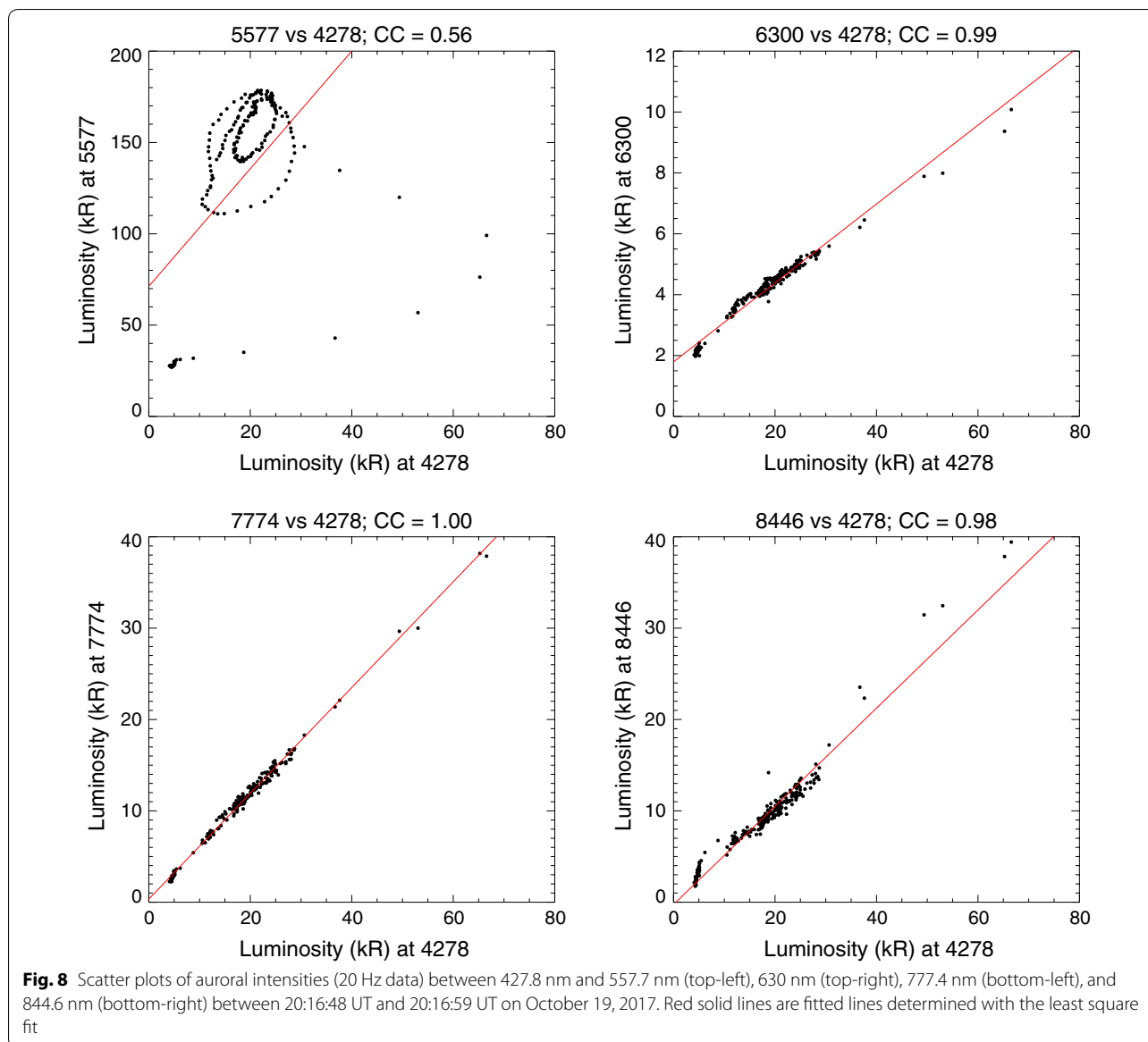
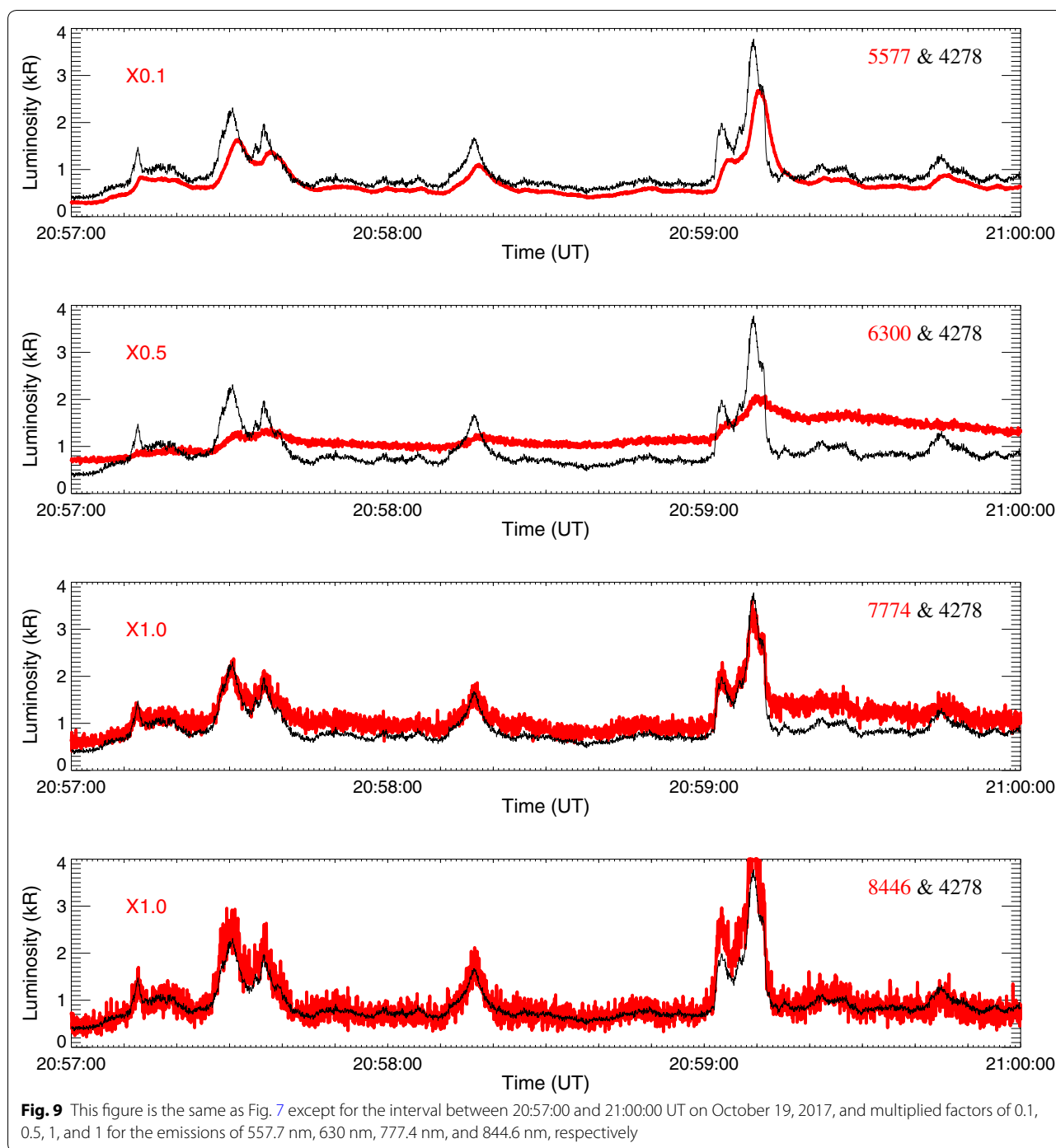


Figure 19 shows temporal variations of the emissions at 557.7, 630, 777.4, and 844.6 nm (red solid lines) together with the 427.8 nm (black solid line) emission for 12 min between 02:12 and 02:24 UT on January 23, 2018. One second average data are presented. All the emissions show pulsating auroral features. The luminosity was relatively dark with about 0.5 kR for all the emissions except for 557.7 nm. A delay can be seen between emissions of 427.8 nm and 557.7 nm, while no delay is seen

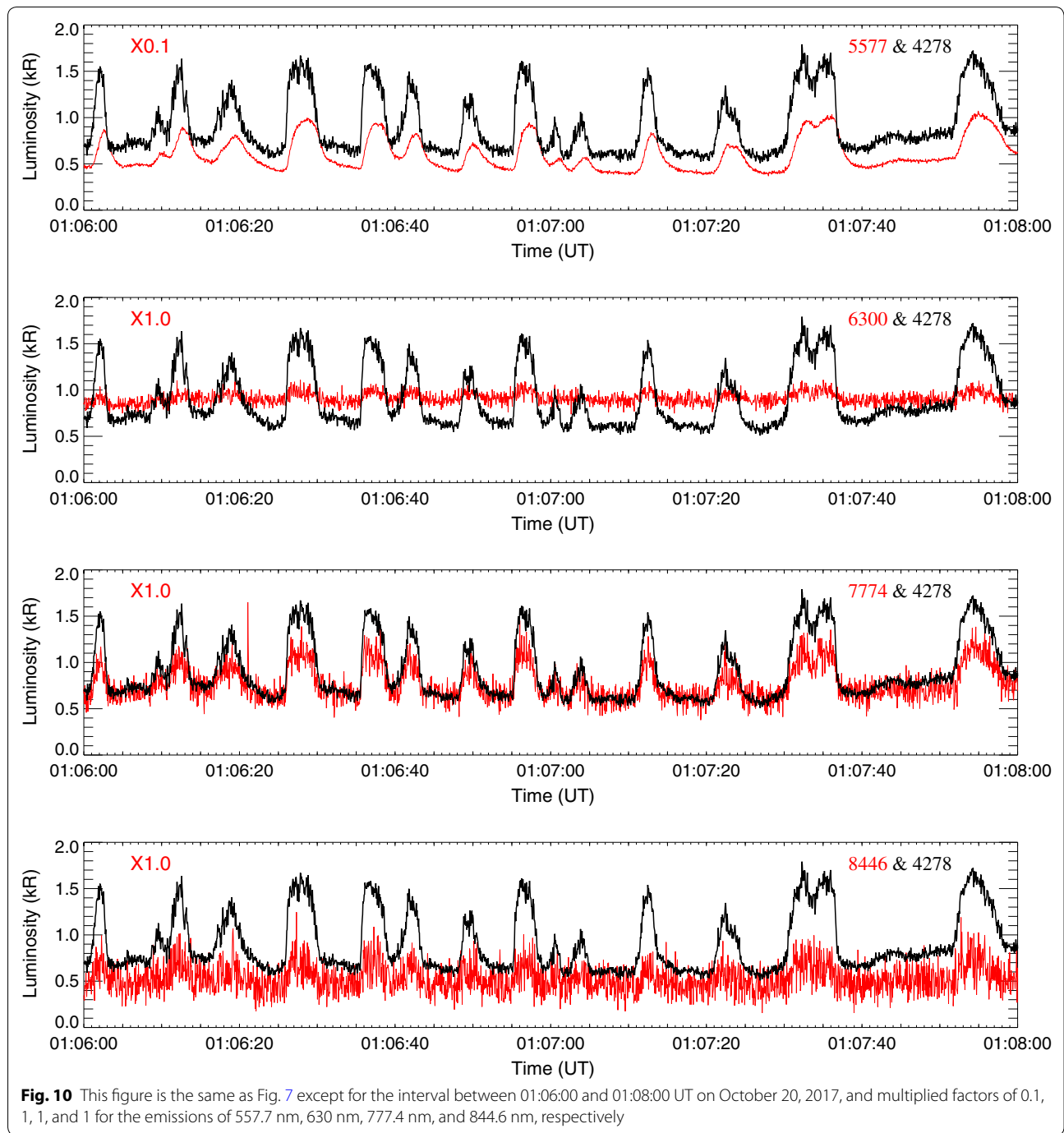
between 427.8 nm and 630 nm. Figure 20 confirms these by scattering plots. The scatter plots between 427.8 nm and the others are well correlated with 427.8 nm emissions except for the 557.7 nm emission. Figure 21 shows spectra for the five emissions derived from 20 Hz data. Several dominant oscillations are seen, but the period of 16.74 s was the most dominant at all the emissions for the time interval.



Discussion

Based on simultaneous observations of the five wavelengths, we have shown temporal variations of the auroral lights of 427.8 nm, 777.4 nm, and 844.6 nm are very similar, and the emission of 557.7 nm is usually delayed (by about 1 s) from that of 427.8 nm. Of particular interest are resemblances of temporal variations sometimes

occurring between 427.8 nm and 630 nm emissions, although it is thought that the emission of 630 nm has a long lifetime (i.e., 40–120 s). Based on High Frequency Active Auroral Research Program (HAARP) ionospheric heating experiments, Pedersen et al. (2008) showed an altitude profile of the effective lifetime of the 630 nm emission; the effective lifetime was below 20 s



at 190 km and rose to over 90 s at an altitude of 350 km. Rapid responses of the 630 nm emission were reported by Eather (1969) and Vallance Jones et al. (1987). Eather

(1969) showed pulsations of the 630 emission with quasi-periods of 2 to about 20 s with relative amplitude of less than 1% in the morning side when 427.8 and 557.7 nm

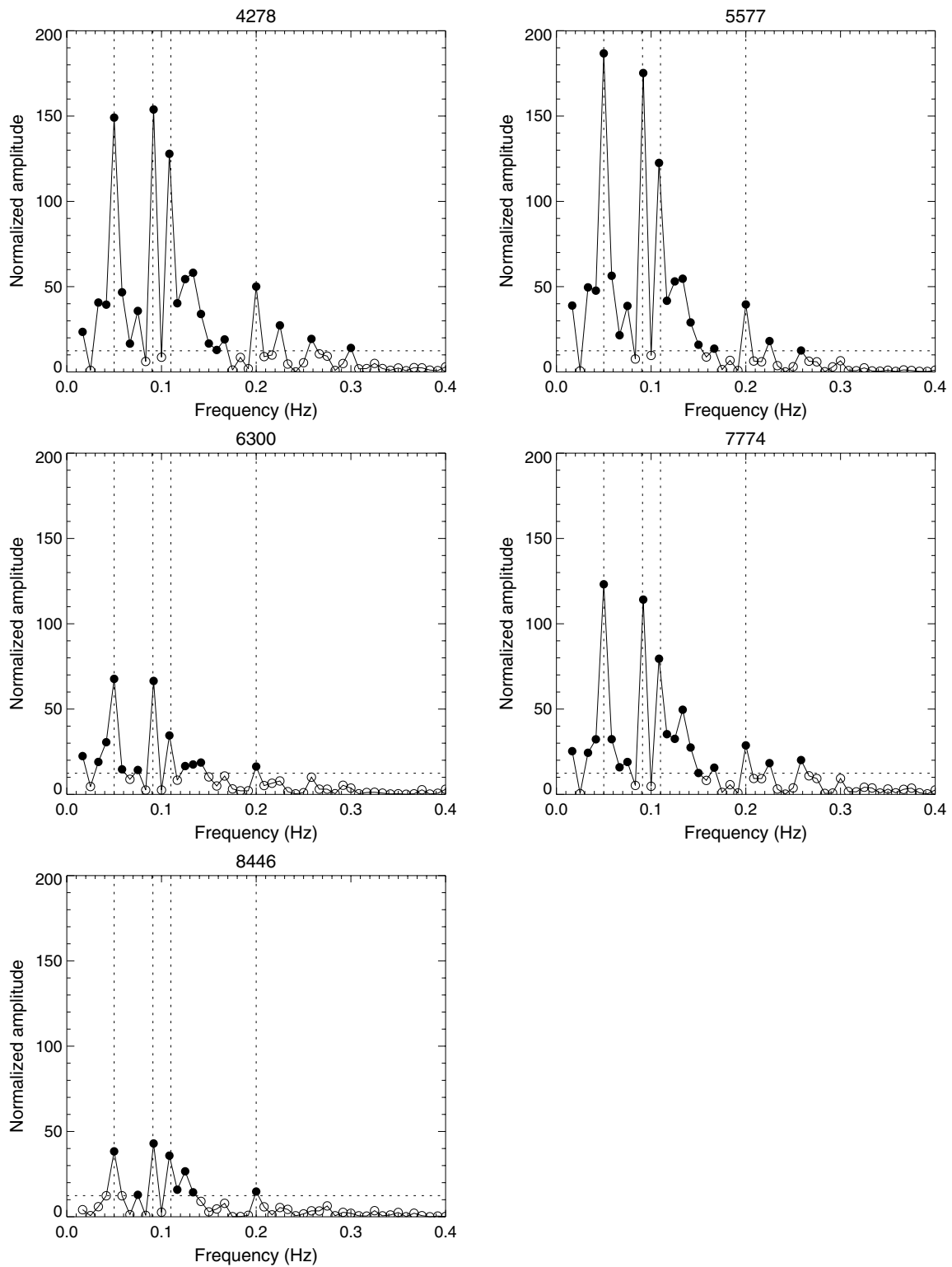


Fig. 11 Spectra for the five emissions between 01:06:00 and 01:08:00 UT on October 20, 2017. The horizontal dashed lines denote the 99% significance level. The vertical dotted lines denote oscillations of 1/5, 1/9.1, 1/11, and 1/20 Hz (i.e., periods being 5, 9.1, 11, and 20 s, respectively). Closed (open) circles denote data whose values are greater (smaller) than the 99% significance level

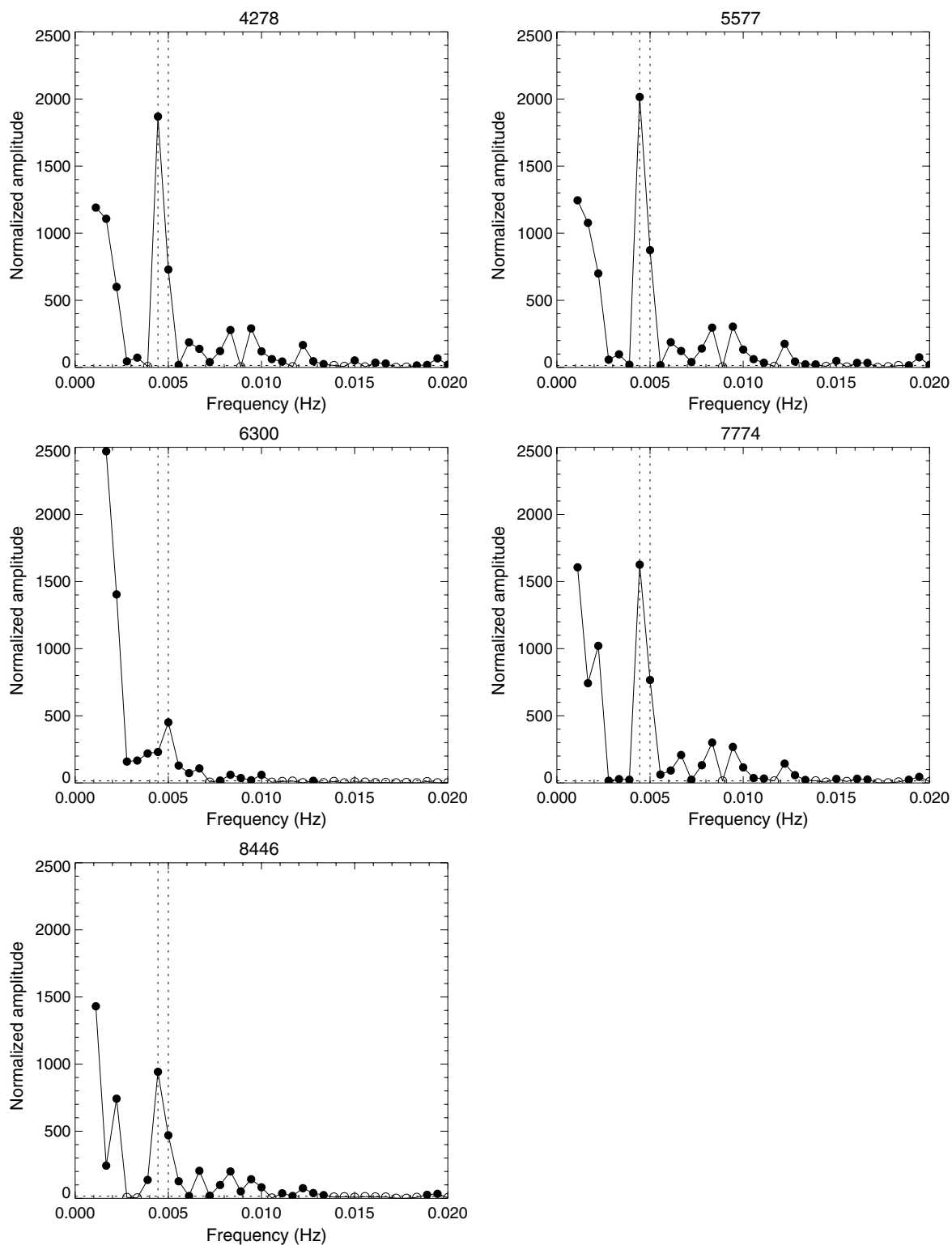


Fig. 12 Spectra for the five emissions between 01:30:00 and 02:00:00 UT on October 20, 2017. The horizontal dashed lines denote the 99% significance level. The vertical dotted lines denote oscillations of 1/200 and 1/225 Hz (i.e., periods being 200 and 225 s, respectively). Closed (open) circles denote data whose values are greater (smaller) than the 99% significance level

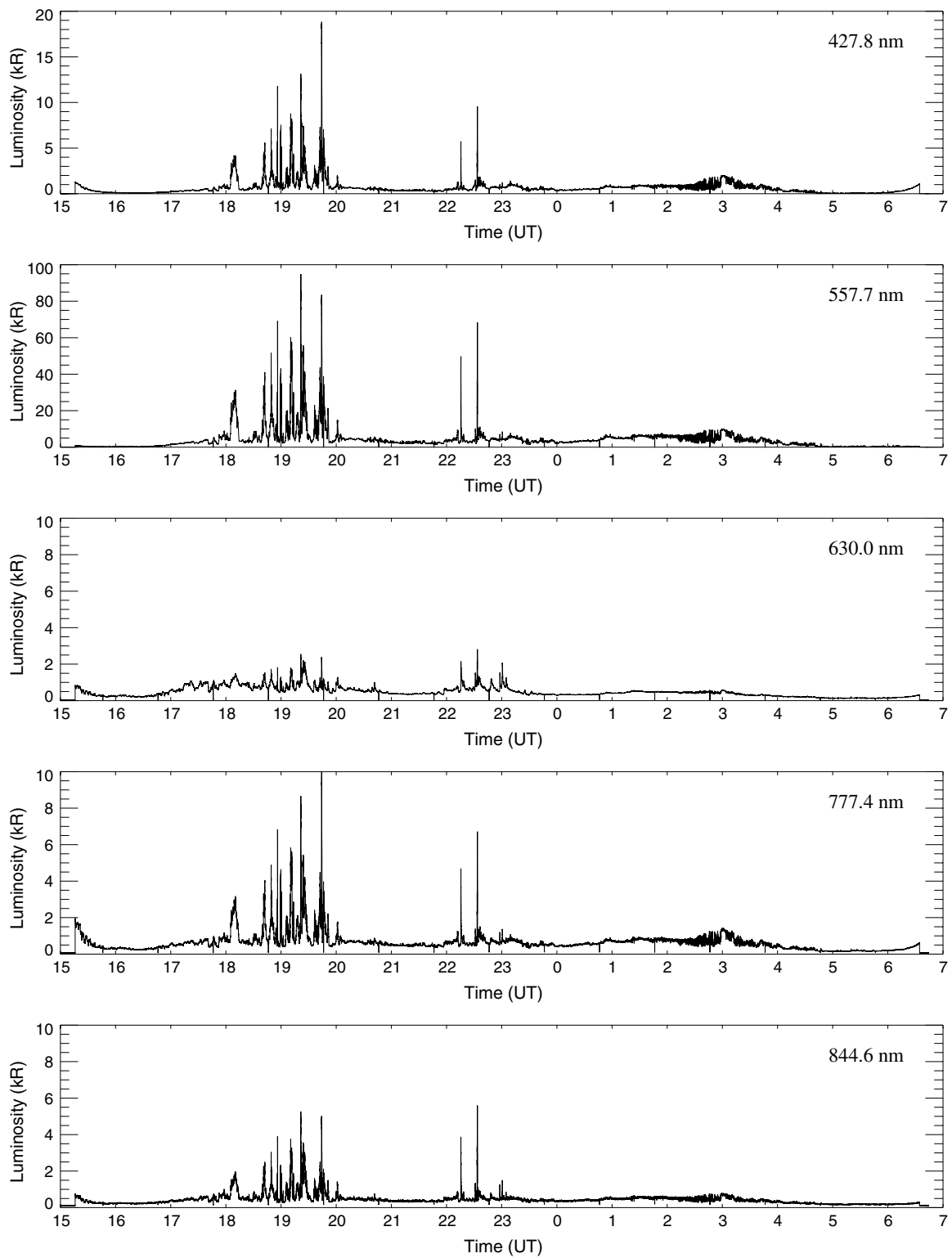


Fig. 13 Temporal variations of the auroral emissions (1 s averaged) obtained with the photometer with five wavelengths between about 15:16 UT on January 22, 2018, and about 06:35 UT on January 23, 2018. The emissions of 427.8 nm, 557.7 nm, 630 nm, 777.4 nm, and 844.6 nm (1 s averaged data) are presented from top to bottom

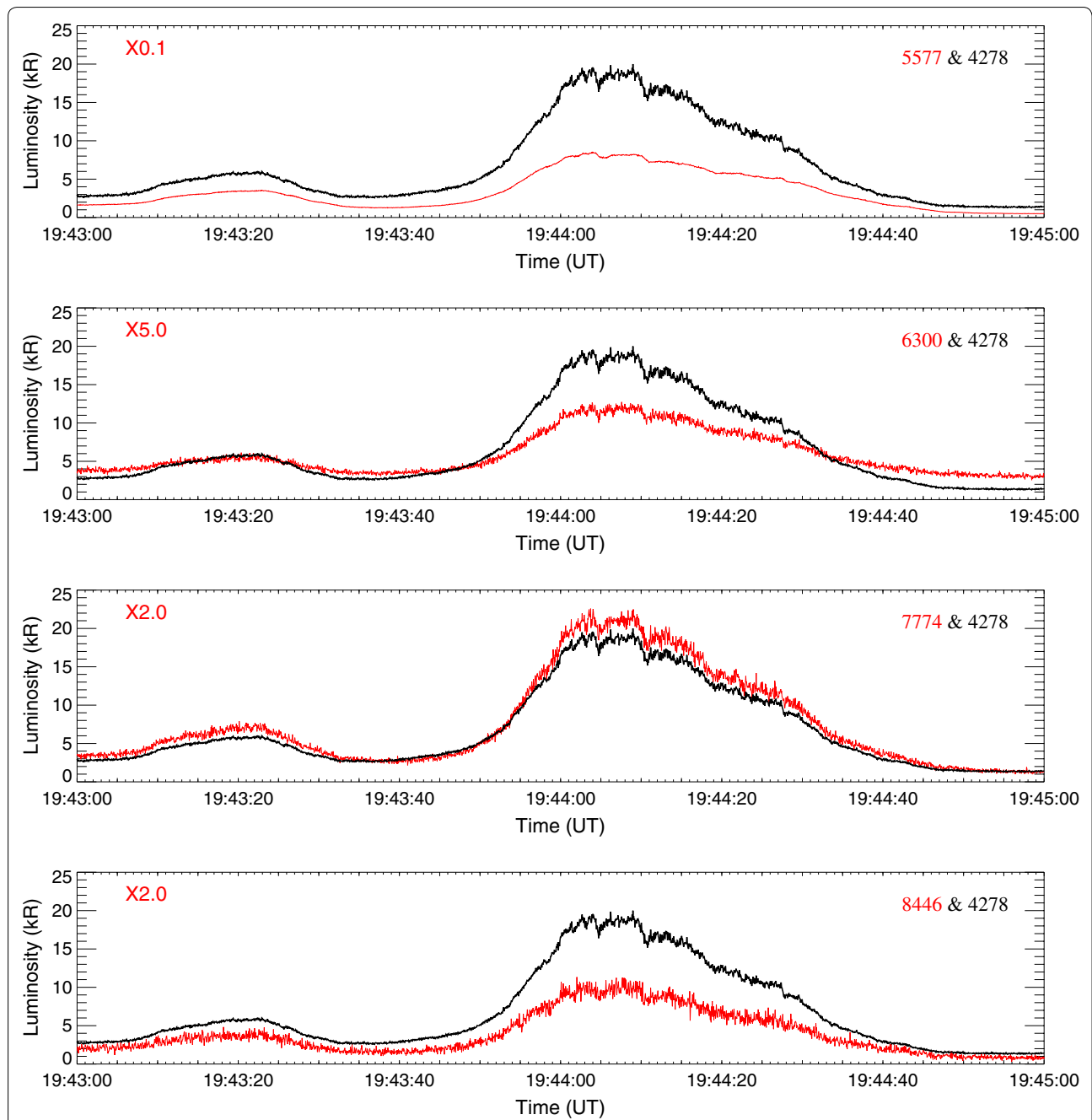
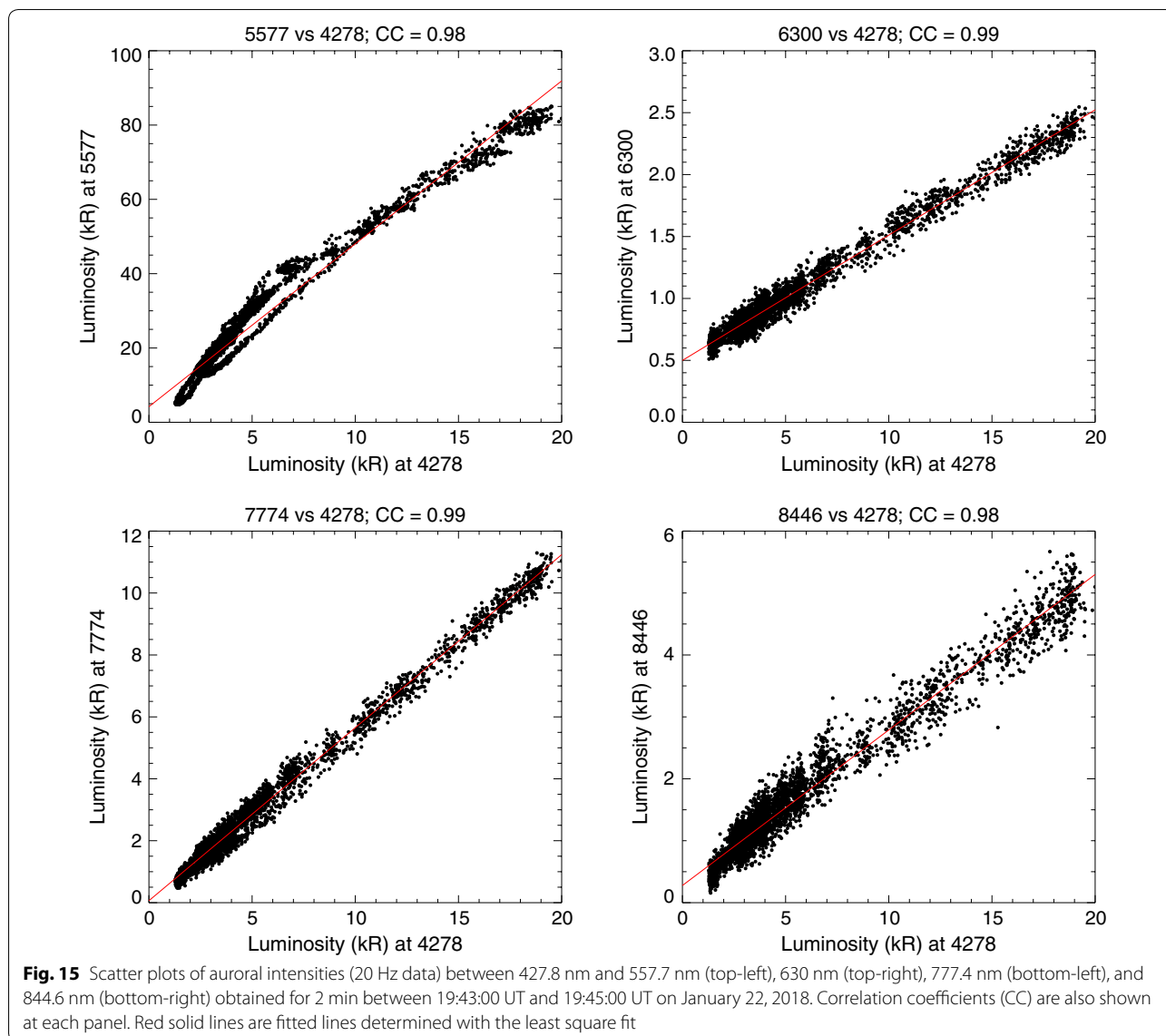


Fig. 14 Comparisons of temporal variations of auroral emissions (20 Hz data used) between 427.8 nm (black) and 557.7 nm, 630 nm, 777.4 nm, and 844.6 nm from top to bottom are presented between 19:43:00 UT and 19:45:00 UT on January 22, 2018. The emission intensities of 557.7 nm, 630 nm, 777.4 nm, and 844.6 nm are multiplied by 0.1, 5, 2, and 2, respectively, and denoted in red solid lines



emissions showed similar pulsations with relative amplitude of 60%. Eather (1969) pointed out these pulsations of the 630 nm emission are due to a quenching effect of $O(^1D)$ occurring below about 170 km (depending on a pulsation period). Liang et al. (2016) showed a red-line (630 nm) pulsating aurora whose magnitude was substantially smaller than that of the concurrent pulsating auroras and pointed out that the altitude range contributing most to the red-line pulsating aurora was systematically lower than that of the steady-state red-line aurora. This idea would explain the pulsation event of the 630 nm emission appearing between 01:06:00 and

01:08:00 UT on October 20, 2017, as shown in Fig. 10, because the portion of the pulsation intensity is small. However, as shown in Fig. 7, a swift rise of the 630 nm emission coordinating with the rapid rise of 427.8 nm cannot be explained well, because most portions of luminosity intensity show a good correlation with that of the 427.8 nm emission. This might suggest the 630 nm line can emanate at much lower heights (below 170 km or lower) than usually expected.

A cause would be due to contamination from other lines. One candidate line is N_2 1PG (10,7) (632.3 nm) band emissions (cf. Ono 1993) which is a prompt

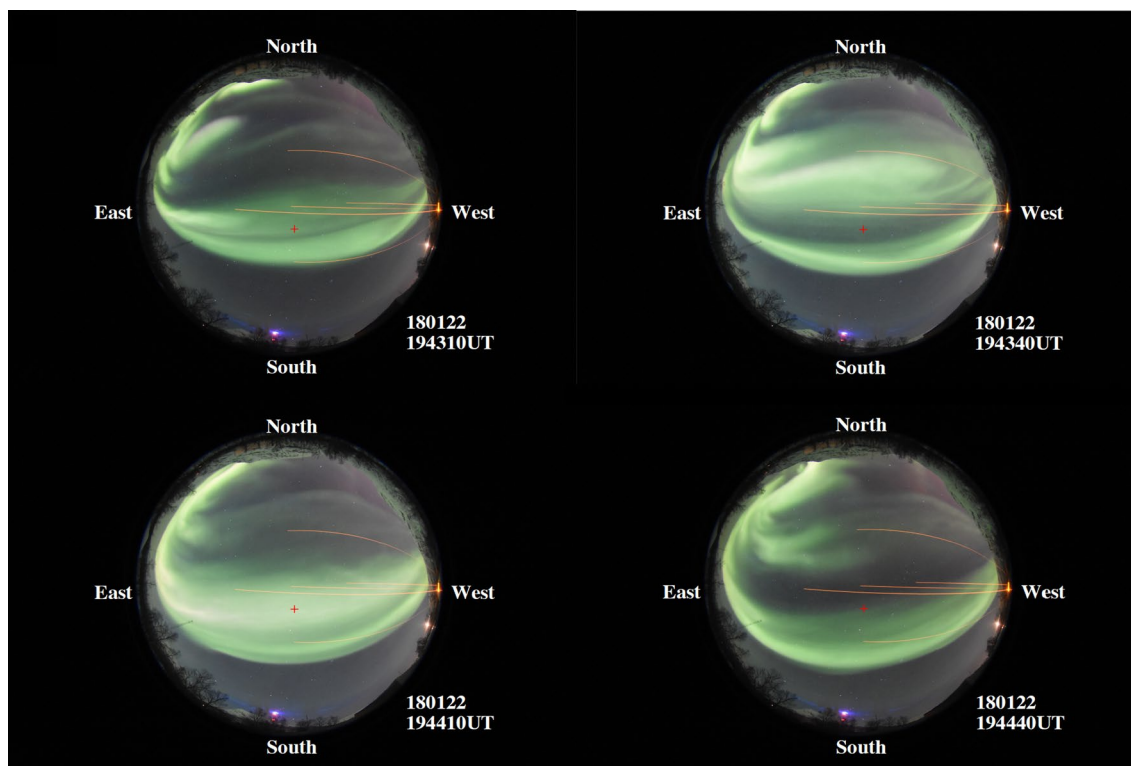
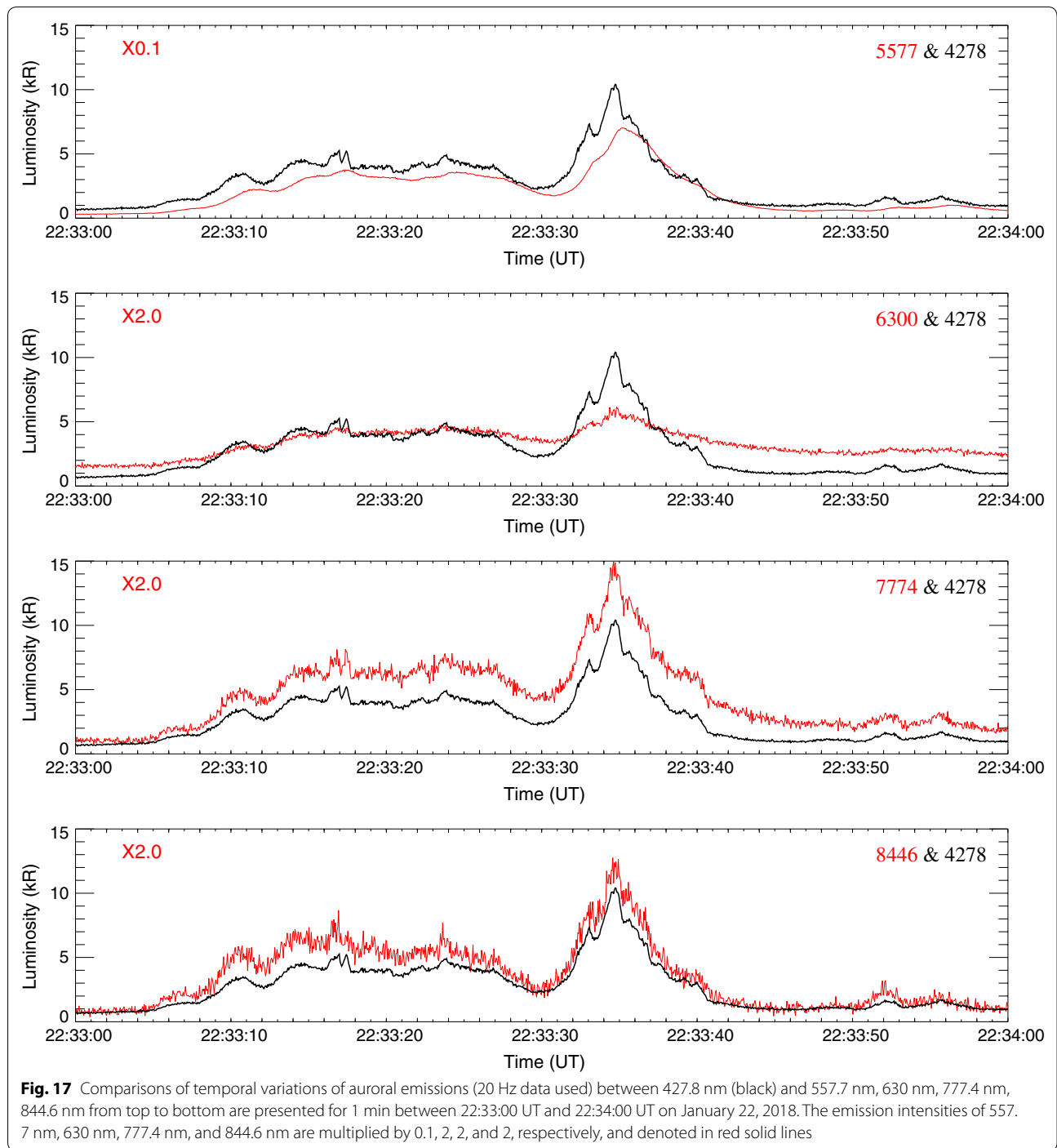


Fig. 16 All-sky images taken with a digital camera (Nikon D7200) every 30 s with exposure time of 8 s between 19:43:10 UT and 19:44:40 UT on January 22, 2018. The field-aligned position, where the photometer was pointed, was indicated by a red plus sign (+)

emission. Figure 22 shows transmissivity (%) of the band-pass filter used for the 630 nm measurements as a function of a wavelength (measured under about 23 °C room temperature). It has a transmissivity of about 1.4% at 632.3 nm, which corresponds to about 1/50 of the transmissivity at 630 nm. The transmissivity has a temperature dependence that tends to shift in the direction of the temperature change which is up with a positive change and down with a negative change. When there is a clear sky, there is a possibility that the room temperature will decrease by up to 20 degrees (i.e., down to around 0 °C). In this case, however, the wavelength dependence shifts to the shorter wavelength, and the transmissivity at 632.3 nm will decrease. On the nights of October 19, 2017, and January 22, 2018, the room temperature was between 16 and 20 °C, and between 11 and 12 °C, respectively.

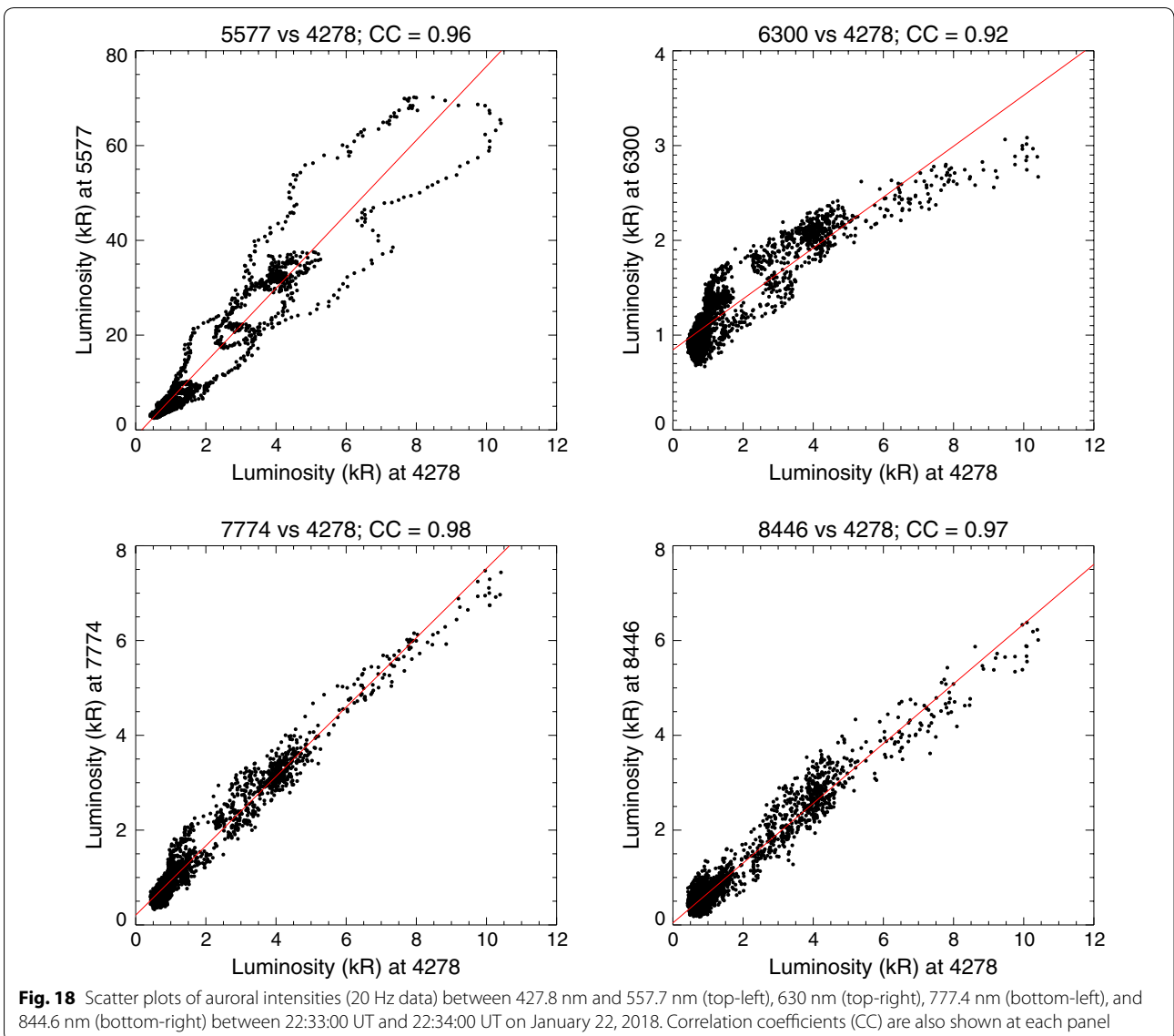
To investigate possible correlations between the two lines of 427.8 nm and 630 nm, 12 nights of data sets (including the two nights already shown) were analyzed when there was (almost) a clear sky over the night and

the auroral activity was high. Table 4 lists the dates. In order to check the response of the 630 nm emission to stepwise changes of the 427.8 nm emission, data events are selected as follows: (1) the rise is greater than 4 kR/sec of the 427.8 nm emission, and (2) 60 s of data starting at the rise time defined by (1) are collected. Here 1 s of averaged data is used. When a next rise occurs within 60 s following the previous one, such an event is treated as one event. In this case, we put the comment “multiple” in Table 4, while the other case is called “single” event. Then, we have investigated dependences of intensity of 427.8 nm. Figures 23 and 24 show data with intensity of 427.8 nm greater and lower than 10 kR, respectively, for the 12 nights. Correlation coefficients (CC) between the emissions of 427.8 and 630 nm are also presented. In cases of the events where the intensity of the 427.8 nm is greater than 10 kR, linear relations can be found between the two emissions, and correlation coefficients on the nights are equal to or greater than 0.90. This would suggest a contamination from 632.3 nm line, at least partly. On the two nights



of January 22 and February 26, 2018, the number of data where the 427.8 nm intensity is greater than 10 kR is low. On the other hand, in the cases where the intensity of the 427.8 nm is smaller than 10 kR, almost

half of events showing poor linear relation between the two lines are seen, and the correlation coefficients become worse (except for 3 nights of January 21 and 22, and February 18, 2018). These cases suggest a delay



of the 630 nm emission. On January 22, 2018, two single events occurred, and on February 18, a single event occurred. For the 2 nights, the good linear relation is found, and the correlation coefficients are high,

indicating the two emissions are well correlated even for an isolated event (i.e., single event). To conclude this, a cause of the swift rise of 630 nm is still unclear. To confirm a possible contamination effect in more

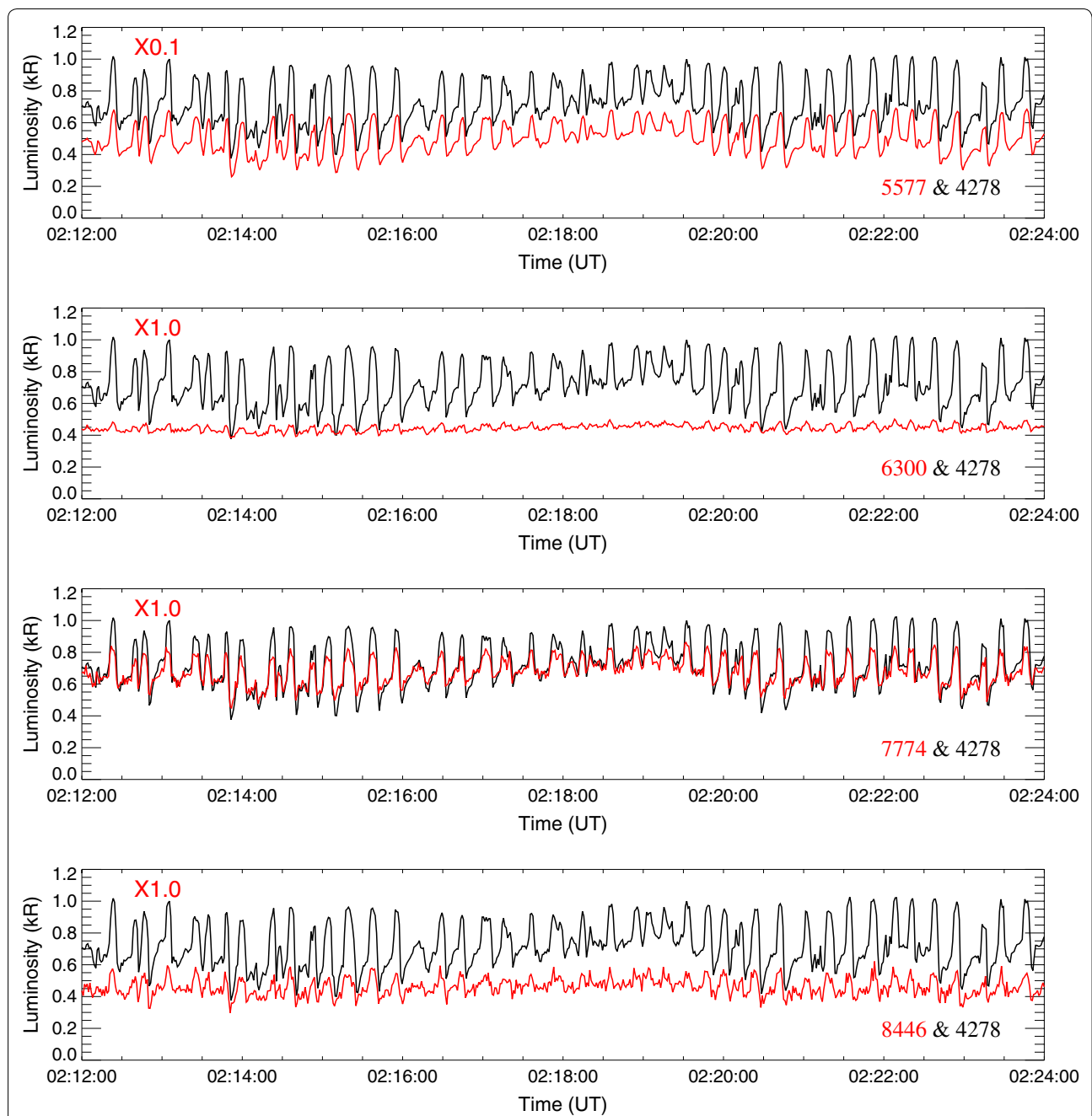


Fig. 19 Comparisons of temporal variations of auroral emissions (1 s data used) between 427.8 nm (black line) and 557.7 nm, 630 nm, 777.4 nm, 844.6 nm from top to bottom are presented for 12 min between 02:12:00 and 02:24:00 UT on January 23, 2018. The emission intensity values of 557.7 nm, 630 nm, 777.4 nm, and 844.6 nm are multiplied by 0.1, 1, 1, and 1, respectively, and shown in red solid lines

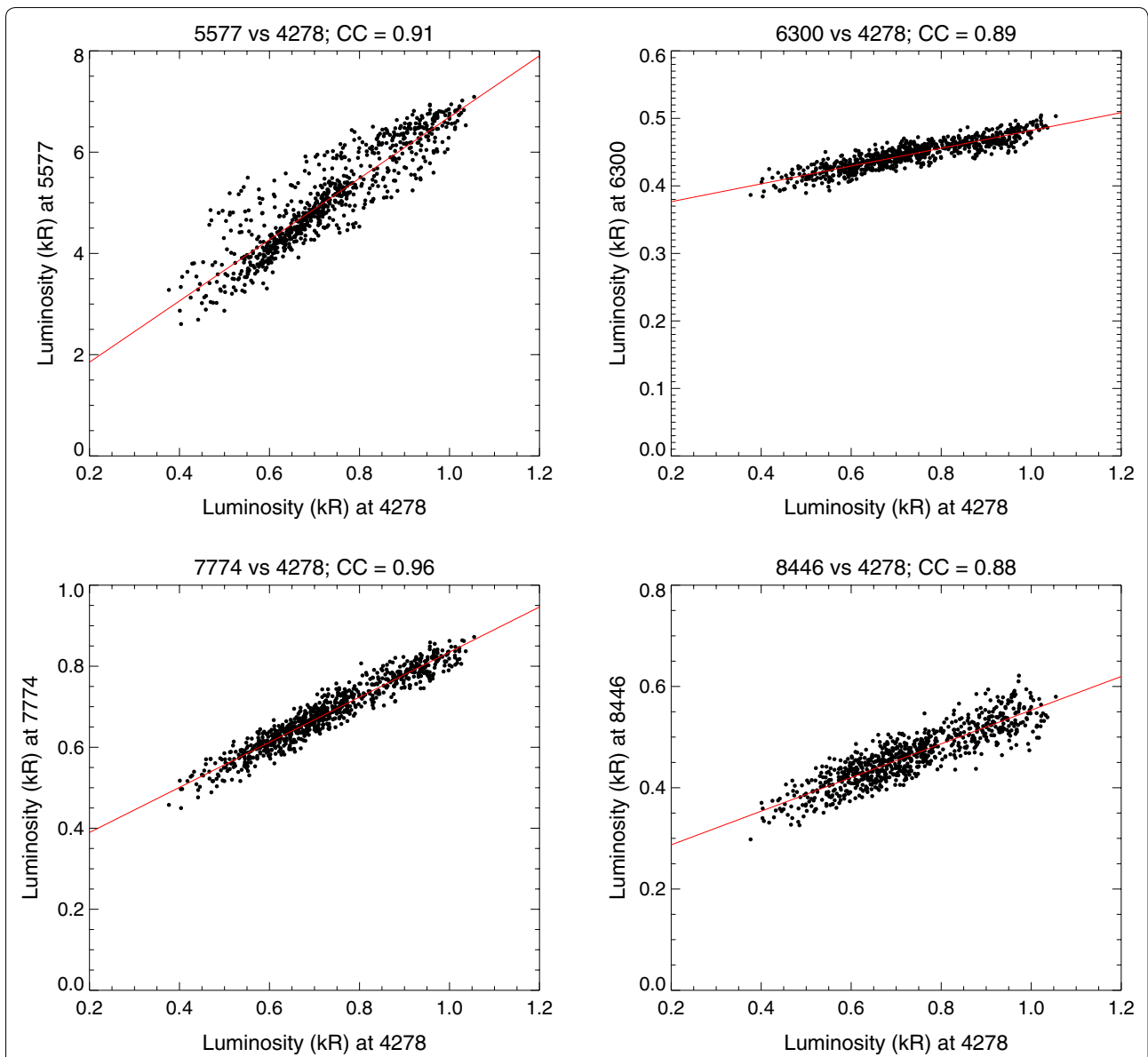


Fig. 20 Scatter plots of auroral intensities (1 s data) between 427.8 nm and 557.7 nm (top-left), 630 nm (top-right), 777.4 nm (bottom-left), and 844.6 nm (bottom-right) between 02:12:00 UT and 02:24:00 UT on January 23, 2018. Correlation coefficients (CC) are also shown at each panel

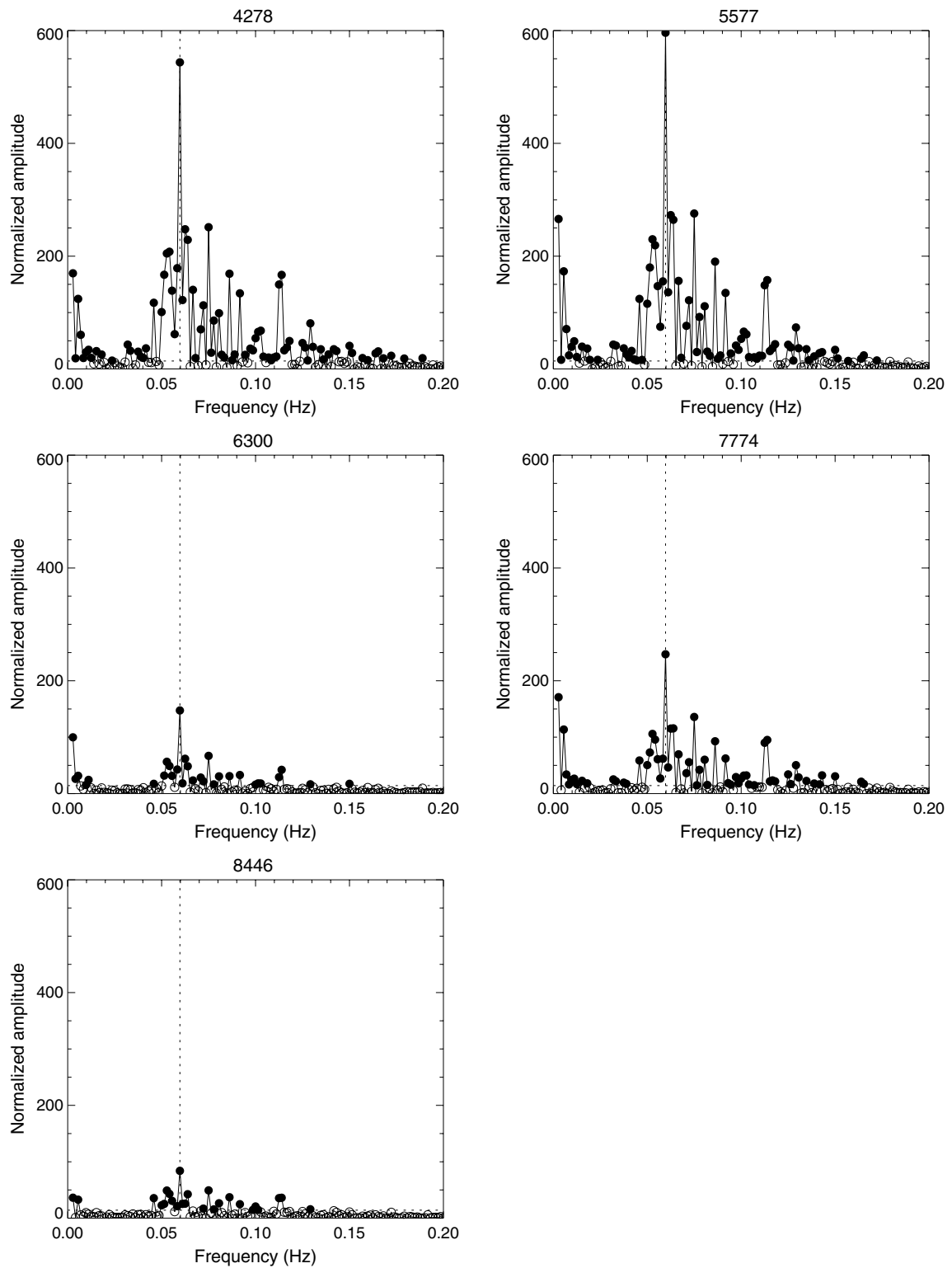


Fig. 21 Spectra of normalized amplitude for the five emissions (20 Hz data) between 02:12:00 UT and 02:24:00 UT on January 23, 2018. The horizontal dashed lines denote the 99% significance level. The vertical dotted lines denote oscillations of 1/16.74 Hz (i.e., period being 16.74 s)

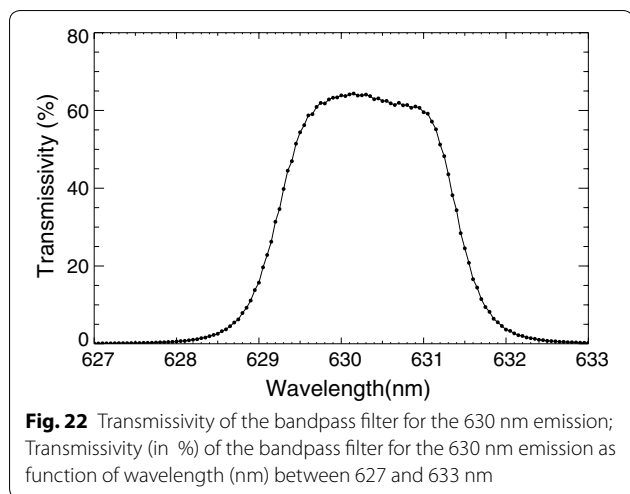


Table 4 List of data sets

Date	Number of events	Comments
September 30, 2017	3	Single, multiple, single
October 19, 2017	2	Single, multiple
October 24, 2017	3	Multiple, multiple, multiple
January 19, 2018	3	Multiple, multiple, multiple
January 21, 2018	3	Multiple, multiple, multiple
January 22, 2018	2	Single, single
January 31, 2018	2	Multiple, multiple
February 16, 2018	2	Multiple, multiple
February 17, 2018	5	All multiple
February 18, 2018	1	Single
February 22, 2018	2	Single, multiple
February 26, 2018	1	Multiple

detail, we need to observe the 632.3 nm emission as well, although it would be a bit difficult for the present photometer.

Correlations between 427.8 nm, 777.4 nm, and 844.6 nm emissions

Linear relationship as well as correlations between three lines of 427.8 nm, 777.4 nm, and 844.6 nm is briefly investigated by analyzing the same data sets as shown in Table 4. Here, data events are selected as follows: (1)

The rise is greater than 4 kR/sec of the 427.8 nm emission (same as before), and (2) 11 s of data starting the rise time defined by (1) minus 1 s are collected. The 20 Hz data are used here. Figure 25 shows scatter plots of between 427.8 nm and 777.4 nm or 844.6 nm emissions with correlation coefficient values. In all the events, almost all data show very good linear relations as well as good correlation coefficients. Of further interest are the correlation coefficients as well as linear relations between 427.8 nm and 777.4 nm emissions, which are slightly better than those between 427.8 nm and 844.6 nm.

Summary and conclusions

A new photometer installed at the EISCAT Tromsø site (69.6°N, 19.2°E) in January 2017 is presented. The new photometer is able to simultaneously observe auroral emissions with five wavelengths (427.8, 557.7, 630, 777.4, and 844.6 nm) at a sampling rate of 400 Hz at the field-aligned position. Such a fast sampling observation presumably enables us to discover fast varying phenomena that have never been possible to identify before; for example, more than 10 Hz rapid modulations are considered to be embedded in a pulsating aurora but have not yet been observationally confirmed. The pointing capability is of vital importance to derive a characteristic energy of the precipitation auroral electrons: The field-aligned measurements are needed because in other directions the observed ratios of two emissions cannot be directly related to energy in a simple way due to spatial ambiguity (cf. Vallance Jones and Gattinger 1990).

The photometer consists of two units: an optical unit and a control unit together with a PC. The photometer was operated at a sampling rate of 400 Hz from September 6, 2017, to March 22, 2018. Some preliminary results on the two nights of October 19, 2017, and January 22, 2018, are presented. Furthermore, we have investigated correlations of temporal variations between 427.8 nm and 630 nm lines. Causes of why the swift rise of the 630 nm emission coordinates with the rapid rise of the 427.8 nm emission are discussed but are concluded to still be unclear. We have suggested two possibilities: the 632.3 nm emission (N_2 1PG(10,

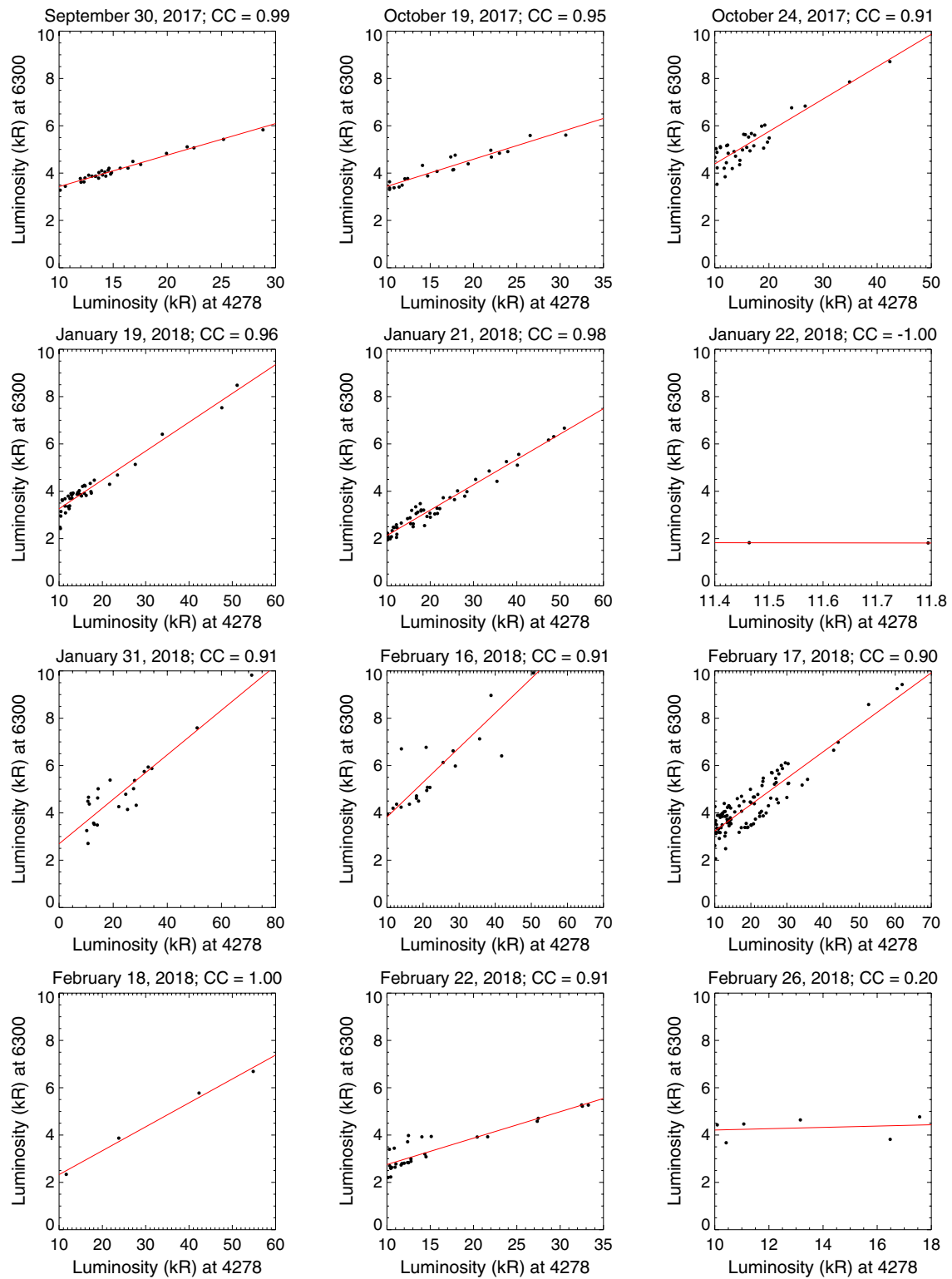


Fig. 23 Scatter plots between 427.8 nm (> 10 kR) and 630 nm emission luminosities; Scatter plots between 427.8 nm and 630 nm emission luminosities for 12 nights where the luminosity of the 427.8 nm is greater than 10 kR

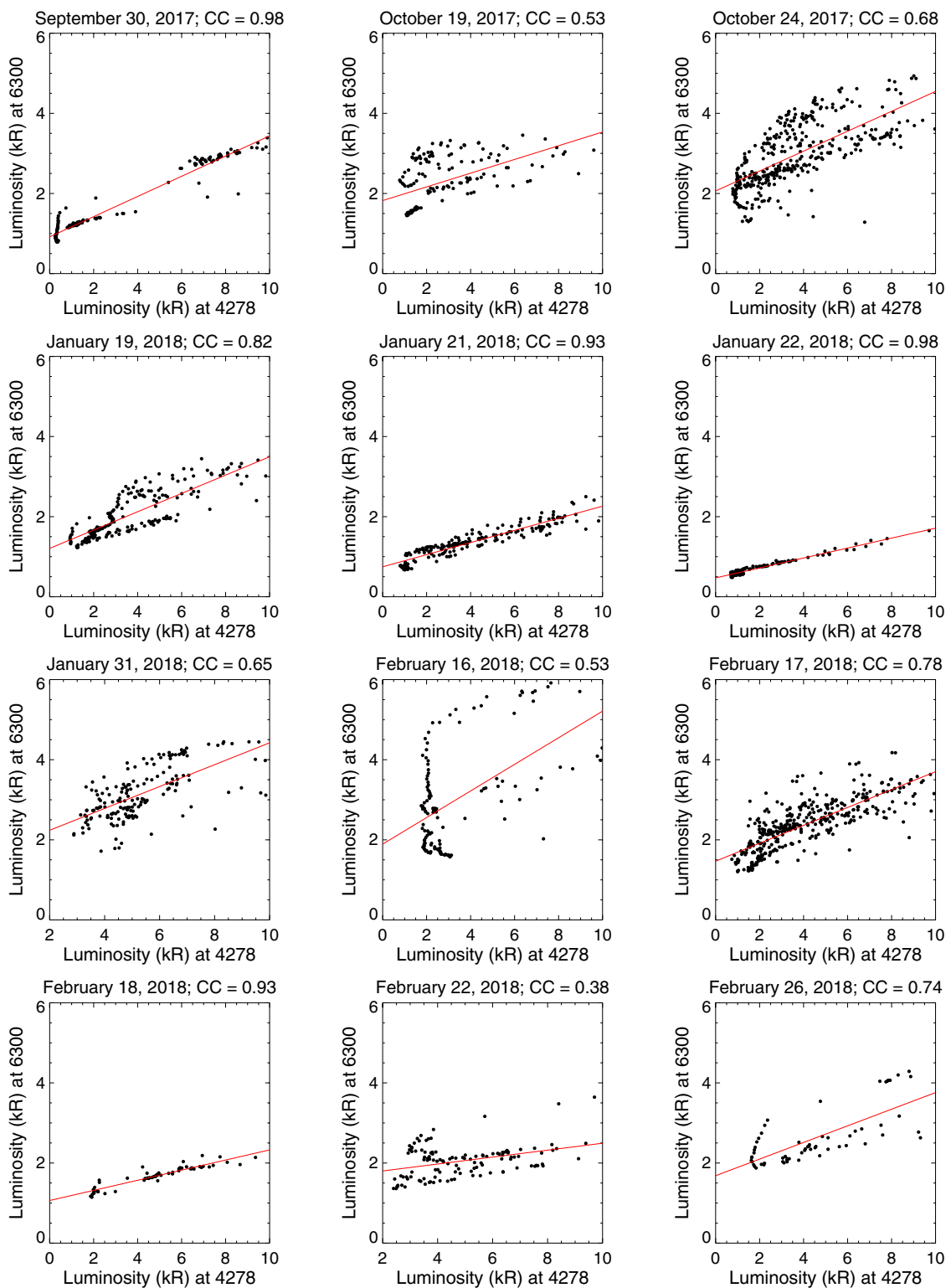


Fig. 24 Scatter plots between 427.8 nm (< 10 kR) and 630 nm emission luminosities; This figure is the same as Fig. 23, except for the conditions where the luminosity of the 427.8 nm intensity is less than 10 kR

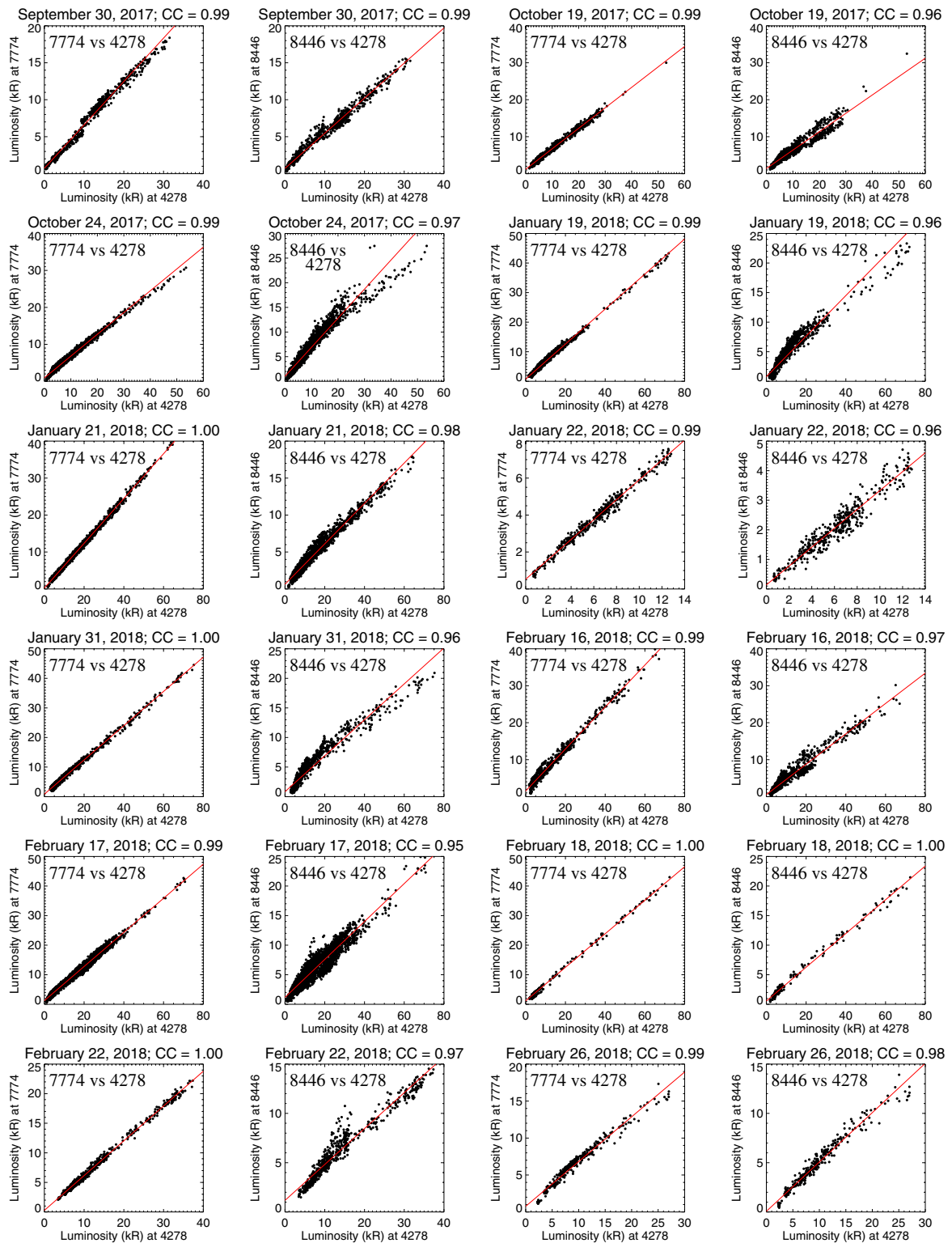


Fig. 25 Scatter plots between 427.8 nm and 777.4 nm/844.6 nm emission luminosities; Scatter plots between 427.8 nm and 777.4 nm/844.6 nm emission luminosities for 12 nights. Red solid lines are fitted lines determined with the least square fit

7)) is a source of contamination, and the 630 nm emission could emanate at much lower heights than usually expected.

Abbreviations

EISCAT: European Incoherent Scatter; FOV: field of view; FWHM: full width at half maximum; HV: high voltage; PC: personal computer; PMT: photomultiplier tube.

Authors' contributions

SN led the research. TK designed and developed the photometer system. KH, RF, TT, and YO contributed to the design and scientific results. AM contributed to the design and supported the operation. CH discussed the scientific results and supported the operation. All authors read and approved the final manuscript.

Author details

¹ Institute for Space–Earth Environmental Research, Nagoya University, Furo-cho, Chikusa-ku, Nagoya, Japan. ² Department of Computer and Network Engineering, The University of Electro–Communications (UEC), Chofu, Japan. ³ National Institute of Polar Research, 10-3, Midori-cho, Tachikawa-shi, Tokyo 190-8518, Japan. ⁴ Tromsø Geophysical Observatory, The Arctic University of Norway, 9037 Tromsø, Norway.

Acknowledgements

The photometer was calibrated using the optical facility at the National Institute of Polar Research (NIPR), Japan. SN thanks Dr. K. Hocke for letting us use his Lomb–Scargle periodogram method routines. This study is partly supported by Grants-in-Aid for Scientific Research (15H05747 and 17H02968) of Japan Society for the Promotion of Science (JSPS). This study is also partly supported by National Institute of Polar Research (NIPR) through General Collaboration Project no. 27-4 and 30-3.

Competing interests

The authors declare that they have no competing interests.

Availability of data materials

<http://www.isee.nagoya-u.ac.jp/~nozawa/photometer/photometer20170201-416hp/index.html>.

Funding

This study is partly supported by Grants-in-Aid for Scientific Research (15H05747 and 17H02968) of Japan Society for the Promotion of Science (JSPS). This study is also partly supported by National Institute of Polar Research (NIPR) through General Collaboration Project no. 27-4 and 30-3.

Publisher's Note

Springer Nature remains neutral with regard to jurisdictional claims in published maps and institutional affiliations.

Received: 30 August 2018 Accepted: 23 November 2018

Published online: 11 December 2018

References

- Adachi K, Nozawa S, Ogawa Y, Brekke A, Hall C, Fujii R (2017) Evaluation of a method to derive ionospheric conductivities using two auroral emissions (428 and 630 nm) measured with a photometer at Tromsø (69.6°N). *Earth Planets Space* 69:90. <https://doi.org/10.1186/s40623-017-0677-4>
- Eather RH (1969) Short-period auroral pulsations in 6300 Å. *J Geophys Res* 74:4998–5004
- Folkstad K, Hagfors T, Westerlund S (1983) EISCAT—an updated description of technical characteristics and operational capabilities. *Radio Sci* 18:867–879
- Gustavsson B, Steen A, Sergienko T, Brandstrom BUE (2001) Estimate of auroral electron spectra, the power of ground-based multi-station optical measurements. *Phys Chem Earth* 26:189–194
- Hecht JH, Christensen AB, Pranke JB (1985) High-resolution auroral observations of the OI(7774) and OI(8446) multiplets. *Geophys Res Lett* 12:605–608
- Hecht JH, Christensen AB, Strickland DJ, Meier RR (1989) Deducing composition and incident electron spectra from ground-based auroral optical measurements: Variations in oxygen density. *J Geophys Res* 94:13553–13563
- Hecht JH, Christensen AB, Strickland DJ, Majeed M, Gattinger RL, Vallance Jones A (1999) A comparison between auroral particle characteristics and atmospheric composition inferred from analyzing optical emission measurements alone and in combination with incoherent scatter radar measurements. *J Geophys Res* 104:33–44
- Hocke K (1998) Phase estimation with the Lomb–Scargle periodogram method. *Ann Geophys* 16:356–358
- Isono Y, Mizuno A, Nagahama T, Miyoshi Y, Nakamura T, Kataoka R, Tsutsumi M, Ejiri MK, Fujiwara H, Maezawa H, Uemura M (2014) Ground-based observations of nitric oxide in the mesosphere and lower thermosphere over Antarctica in 2012–2013. *J Geophys Res* 119:7745–7761. <https://doi.org/10.1002/2014JA019881>
- Kalogerakis KS, Slangier TG, Kendall EA, Pedersen TR, Kosch MJ, Gustavsson B, Rietveld MT (2009) Remote oxygen sensing by ionospheric excitation (ROSIE). *Ann Geophys* 27:2183–2189
- Krassovsky VI, Shefov NN, Yarin VI (1962) Atlas of the airglow spectrum 3000–12400 Å. *Planet Space Sci* 9:883–915
- Lanchester BS, Ashrafi M, Ivchenko N (2009) Simultaneous imaging of aurora on small scale in OI (777.4 nm) and N21P to estimate energy and flux of precipitation. *Ann Geophys* 27:2881–2891
- Liang J, Donovan E, Jackel B, Spanswick E, Gillies M (2016) On the 630 nm red-line pulsating aurora: red-line emission geospace observatory observations and model simulations. *J Geophys Res* 121:7988–8012. <https://doi.org/10.1002/2016JA022901>
- Lummerzheim D, Rees MH, Romick GJ (1990) The application of spectroscopic studies of the aurora to thermospheric neutral composition. *Planet Space Sci* 38:67–78
- Meier RR, Strickland DJ, Hecht JH, Christensen AB (1989) Deducing composition and incident electron spectra from ground-based auroral optical measurements: a study of auroral red line processes. *J Geophys Res* 94:13541–13552
- Niciejewski RJ, Meriwether JW Jr, Vallance Jones A, Gattinger RL, Valladares CE, Wickwar VB, Kelly J (1989) Ground-based observations of O₂⁺ 1N band enhancements relative to N₂⁺ 1N band emission. *Planet Space Sci* 37:131–143
- Ono T (1993) Derivation of energy parameters of precipitating auroral electrons by using the intensity ratios of auroral emissions. *J Geomagn Geoelectr* 45:455–472
- Ono T, Hirasawa T (1992) An apparent lifetime of auroral 630.0 nm (OI) emissions. *J Geomagn Geoelectr* 44:91–108
- Oyama S, Watanabe T, Fujii R, Nozawa S, Tsuda TT (2013) Estimation of the layered ionospheric conductance using data from a multi-wavelength photometer at the European Incoherent Scatter (EISCAT) radar site. *Antarct Rec* 57(3):339–356
- Pedersen T, Esposito R, Kendall E, Sentman D, Kosch M, Mishin E, Marshall R (2008) Observations of artificial and natural optical emissions at the HAARP facility. *Ann Geophys* 26:1089–1099
- Press WH, Rybicki GB (1989) Fast algorithm for spectral analysis of unevenly sampled data. *Astrophys J* 338:277–280
- Rees MH, Luckey D (1974) Auroral electron energy derived from ratio of spectroscopic emissions. I—model computations. *J Geophys Res* 79:5181–5186
- Robinson RM, Vondrak RR (1994) Validation of techniques for space based remote sensing of auroral precipitation and its ionospheric effects. *Space Sci Rev* 69:331–407
- Scourfield NWJ, Parsons NR, Dennis LP, Innes WF (1971) Effective lifetime of O(¹S) in Pulsating Aurora. *J Geophys Res* 76:3692–3699
- Semeter J, Lummerzheim D, Haerendel G (2001) Simultaneous multispectral imaging of the discrete aurora. *J Atmos Sol-Terr Phys* 63:1981–1992
- Strickland DJ, Meier RR, Hecht JH, Christensen AB (1989) Deducing composition and incident electron spectra from ground-based auroral optical measurements: theory and model results. *J Geophys Res* 94:13527–13539
- Takahashi T, Nozawa S, Tsuda TT, Ogawa Y, Saito N, Hidemori T, Kawahara TD, Hall C, Fujiwara H, Matuura N, Brekke A, Tsutsumi M, Wada S, Kawabata T,

- Oyama S, Fujii R (2015) A case study on generation mechanisms of a sporadic sodium layer above Tromsø (69.6°N) during a night of high auroral activity. *Ann Geophys* 33:941–953
- Tsuda T, Yamamoto M, Hashiguchi H, Shiokawa K, Ogawa Y, Nozawa S, Miyaoka H, Yoshikawa A (2016) A proposal on the study of solar-terrestrial coupling processes with atmospheric radars and ground-based observation network. *Radio Sci.* <https://doi.org/10.1002/2016rs006035>
- Turunen E, Verronen PT, Seppala A, Rodger CJ, Clilverd MA, Tamminen J, Enell C-F, Ulich T (2009) Impact of different energies of precipitating particles on NO_x generation in the middle and upper atmosphere during geomagnetic storms. *J Atmos Sol-Terr Phys* 71:1176–1189
- Vallance Jones A (1974) *Aurora, geophysics and astrophysics monographs*, 9, published by D. Reidel Publishing Company, Holland
- Vallance Jones A, Gattinger RL (1990) Auroral spectroscopy and its applications to the characterization of primary particle fluxes. *J Geomagn Geoelectr* 42:1385–1410
- Vallance Jones A, Gattinger RL, Shih P, Meriwether JW, Wickwar VB, Kelly J (1987) Optical and radar characterization of a short-lived auroral event at high latitude. *J Geophys Res* 92:4575–4589
- Vondrak RR, Sears RD (1978) Comparison of incoherent scatter radar and photometric measurements of the energy distribution of auroral electrons. *J Geophys Res* 83:1665–1667

Submit your manuscript to a SpringerOpen[®] journal and benefit from:

- ▶ Convenient online submission
- ▶ Rigorous peer review
- ▶ Open access: articles freely available online
- ▶ High visibility within the field
- ▶ Retaining the copyright to your article

Submit your next manuscript at ▶ springeropen.com
